# Chapter 5

# Energy Redistribution: Fragmentation of $C_{60}$ after Femtosecond Laser Excitation

Fragmentation is one of the fundamental mechanisms to release excess energy in molecular systems and can be defined as the separation of a collective into smaller pieces. For small systems, this involves breaking particular chemical bonds of the molecule and is termed dissociation. For larger systems, particularly clusters, where energy can be efficiently stored, one can talk of a statistical process: evaporation. The fragmentation of $C_{60}$ has historically been discussed in terms of evaporation, even though the system is strongly bound together. Nevertheless the photo-fragmentation of $C_{60}$ has shown many interesting features, which have been explained successfully through statistical processes, which given the time scale of excitation (typically nanoseconds) and measurement (typically microseconds) is sufficient. However, with intense fs laser sources, the statistical explanations may no longer hold. Recent theoretical simulations have shown fragmentation occurring on the femtosecond time scale, which is faster than statistical processes would allow. In this chapter, time resolved pump-probe spectroscopy is used to experimentally investigate fragmentation dynamics of $C_{60}$ after excitation with short, intense laser excitation.

First, an overview of fragmentation, as well as ionization and energy redistribution, of $C_{60}$ either measured or theoretically treated will be presented. Although numerous studies have considered fragmentation and ionization of $C_{60}$ after nanosecond laser irradiation or collisional excitation, few works consider the fragmentation by femtosecond laser irradiation.

The second part of the chapter highlights new experimental results concerning

fragmentation after intense femtosecond laser pulse interaction with $C_{60}$. The consequences of this interaction are monitored by time of flight spectroscopy both conventionally (without spatial resolution) and with position sensitive detection. Laser excitation occurs either with single femtosecond laser pulses or with two laser pulses with a defined delay.

## 5.1 Introduction : Ionization and fragmentation of $C_{60}$

Pioneering experiments on the photo-physics of fullerenes have illuminated very interesting ionization and fragmentation properties [KHB85] [OHC88]. In those experiments, mass spectra resulting from $C_{60}$ excited with ns laser pulses contain two regions, distinguished by their mass peak separation. For fragments of more than 32 carbon atoms, the separation between mass peaks is 2 carbon atoms. These fragments have a similar 3-D cage-like structure as $C_{60}$. The mass peaks of the lighter fragments with less than 30 atoms are separated by 1 carbon atom. Two structures make up this population. For systems with less than 9 atoms, linear chains dominate. Clusters between 9 and 30 atoms exhibit a monocyclic ring structure. From the first photo-fragmentation experiments[OHC88], it has been suggested that a sequential loss of $C_2$ units is not energetically favorable, thus chains and rings of 4, 6, etc., atoms are ejected from the fullerene cage after laser excitation. This fragmentation process has been described as an unzipping mechanism. However, the fragmentation of fullerenes is presently understood to be dependent on the internal energy reached in the excitation process. In low excitation processes, the dominant channel is sequential $C_2$ loss. As the internal energy crosses a threshold of about 80 eV (determined from electron impact), multiple fragmentation of the cage is expected [Cam03]. The timescale of statistical fragmentation is determined by the internal energy.

After the initial fragmentation, internal energies of the produced fragments (daughters) can be high enough to cause further fragmentation (granddaughter). The amount of statistical fragmentation is dependent on the amount of energy coupled into the system. Further fragmentation of heavy fullerene-like fragments is understood to be neutral $C_2$ emission. No experimental evidence for neutral $C_4$ emission exists. For all carbon clusters with less than 20 atoms, fragmentation proceeds pre-

dominantly through $C_3$ loss [GMJ86]. Both of these fragmentation pathways are the most energetically favorable for the particular mass size.

The time scales of fragmentation into daughter/granddaughter fragments have been studied with empirical molecular dynamic simulations. Fragmentation in this model is considered only from internal vibrational energy and indicates that a total internal energy of 150 eV can produce up to four fragments on a 20 ps time scale [HEF95]. The initial fragmentation processes produced a ring and chain occurring within a 5 ps time scale. Although this is an oversimplification of the fragmentation process, it can be concluded that the ps fragmentation of $C_n$ for n>2 can be an important channel for relaxation from highly excited systems.

More recent measurements have studied ion-ion coincidence of collision induced dissociation of $C_{60}^-$ [VHC98]. Colliding 75 keV $C_{60}^-$ with $H_2$ produces positively charged fragments, which are then detected in coincidence. Both odd and even sized small fragments are found to be in coincidence with the even numbered heavier partners (fullerenes). This is supports a model of a successive fragmentation of the non-fullerene lighter fragment. However, due to the long sampling time (3 $\mu$s after collision) many fragmentation events can take place. Thus far, no coincident measurements of photo-fragmentation products have been performed.

To understand the neutral fragments produced in laser induced photo-fragmentation of $C_{60}$, Lykke performed "post-ionization" experiments [Lyk95] by initiating fragmentation with an Nd:YAG (266 nm) laser and subsequently ionizing with an XUV (94.54 nm) laser pulse 50-300 ns later. To produce $C_{60}^+$ in the gas phase, Lykke uses laser desorption. As is evidenced by the $C_{60}$ peak in the TOF mass spectrum resulting from laser desorption alone, these clusters are electronically and vibrationally hot before the fragmentation laser interacts with the clusters. From the results, it is concluded that neutral C, $C_2$, $C_3$, and $C_4$ are all present in the direct fragment distribution of fullerenes (not from fragmentation of fragments). However, one could argue that 50 ns allows enough time for significant fragmentation from fullerenes with high internal energy as found in molecular dynamic calculations [HEF95].

Fragmentation of fullerenes from ns-laser sources has been successfully modelled from statistical considerations. Femtosecond laser excitation, however, deposits energy into the system faster than the electronic-vibrational coupling time and introduces the possibility of non-statistical fragmentation mechanisms.

The fragmentation pattern with fs laser pulses is significantly different from the fragmentation observed with nanosecond (or even ps) laser irradiation of similar laser

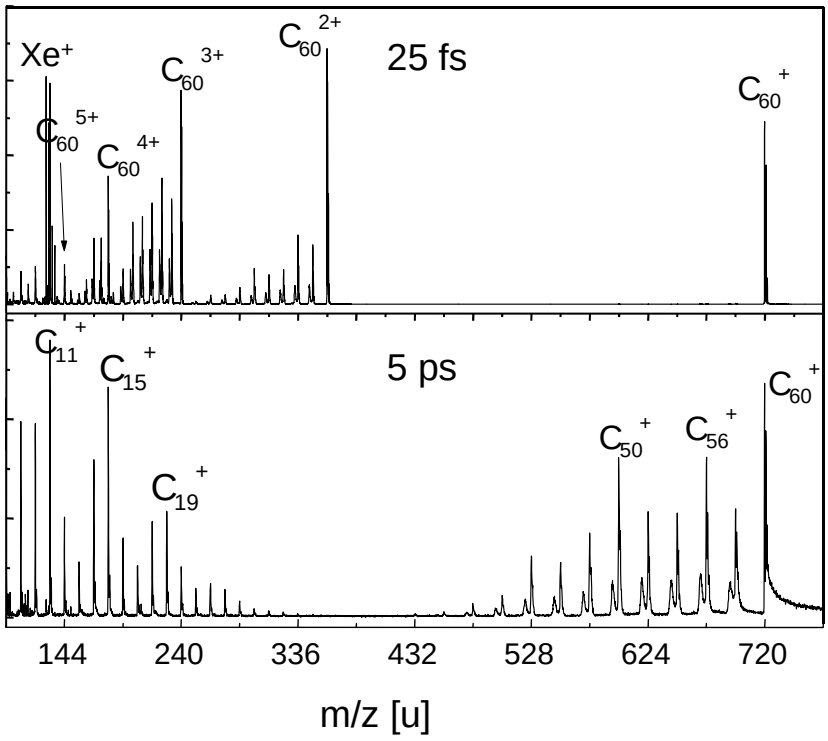


Figure 5.1: *Comparison of mass spectra obtained with equal fluence pulses (20 J/cm$^2$) of different pulse durations a.) 25 fs and b.) 5 ps (from [CHH01]).*

fluence as is shown in Fig. 5.1. The mass spectra have been measured with a reflectron time-of-flight (ReTOF) for two different laser pulse durations: 25 fs and 5 ps. The time of flight has been converted to the mass to charge ratio in atomic mass units. For the 25 fs pulse duration, multiply charged $C_{60}^{z+}$, up to charge state z = 5, were detected. Significant fragmentation was observed with excitation by high intensity laser irradiation (>8*10$^{13}$ W/cm$^2$) for charge states z>1. In addition, metastable fragmentation (as defined in chapter 2) is present in a ReTOF spectrum, which is similar to the ps or ns mass spectrum. This indicates that a significant amount of energy is coupled into the vibrational system from the electronic excitation. However, the increase in internal energy is likely to not result from the same process as for nanosecond irradiation, in which many absorption and relaxation events can take place during the duration of the laser pulse.

The 5 ps laser pulse produces a mass spectrum (Fig. 5.1b.) with a typical bimodal pattern observed in the first photo-fragmentation experiments with nanosecond laser sources [OHC88]. Significant amounts of charged small fragments as well as heavy

fullerene fragments are produced in the fragmentation process. No multiple ionization of $C_{60}$ is observed. Additionally, a pronounced tail on the $C_{60}$ peak toward higher mass is detected. This tail is due to delayed ionization of $C_{60}$ [CUH91].

The two spectra in Fig. 5.1 highlight the importance of energy redistribution processes encountered by changing the time scale of laser excitation. The competition between ionization and energy redistribution is important for understanding fragmentation of $C_{60}$. The time scales of energy redistribution from electronic to vibrational degrees of freedom dictate where the excess energy is located in the system (electronic or vibrational degrees of freedom) and ionization and fragmentation are competing energy-loss channels. Radiative energy loss is not considered here as the effect is generally insignificant on the timescale considered here.

First experimental results concerning the time scales of energy redistribution were obtained through the interpretation of the photoelectron and photoion spectra measured with different excitation pulse durations. As the pulse duration is changed from 25 fs to 5 ps, a transition in the ionization mechanism occurs between predominantly above threshold ionization (ATI) to statistical emission processes [CHH00]. Photoelectron (left) and photoion (right) spectra are shown in Fig. 5.2.

Each photoelectron spectrum exhibits the signal versus the electron kinetic energy, which has been converted from the TOF distribution. The mass spectra show the signal versus time-of-flight. For pulse durations less than 70 fs, photo-electron spectra are characterized by a series of peaks separated by the photon energy, which is attributed to ATI as shown in Fig. 5.2a, left. The corresponding mass spectra show primarily the parent ions, $C_{60}^{+}$ and $C_{60}^{++}$, with little or no fragmentation, Fig. 5.2a, right. The initial electronic excitation is found to couple to an electronic bath on a sub 50 fs time scale. For pulse durations between 100 fs and 500 fs, initial electronic excitation has coupled to the electronic bath and begun to couple to vibrational degrees of freedom. As a result, a very hot photoelectron spectrum is measured corresponding to the electronically hot molecules (Fig. 5.2b and c, left), as electron emission occurs through a statistical process from the excited electronic bath. Although significant fragmentation is not produced for 100 fs pulse durations (Fig. 5.2b, right), it is a prominent feature at 500 fs (Fig. 5.2c, right), as the electronic energy couples into the vibrational system on this time scale. Modelling using, in addition, Penning ionization data has shown that the time constant is $\sim$ 240 fs [HHC03]. With 5 ps pulse duration excitation, the electronic system has cooled as evidenced in the narrow photoelectron spectra(Fig. 5.2d, left), and a bimodal distribution of singly charged

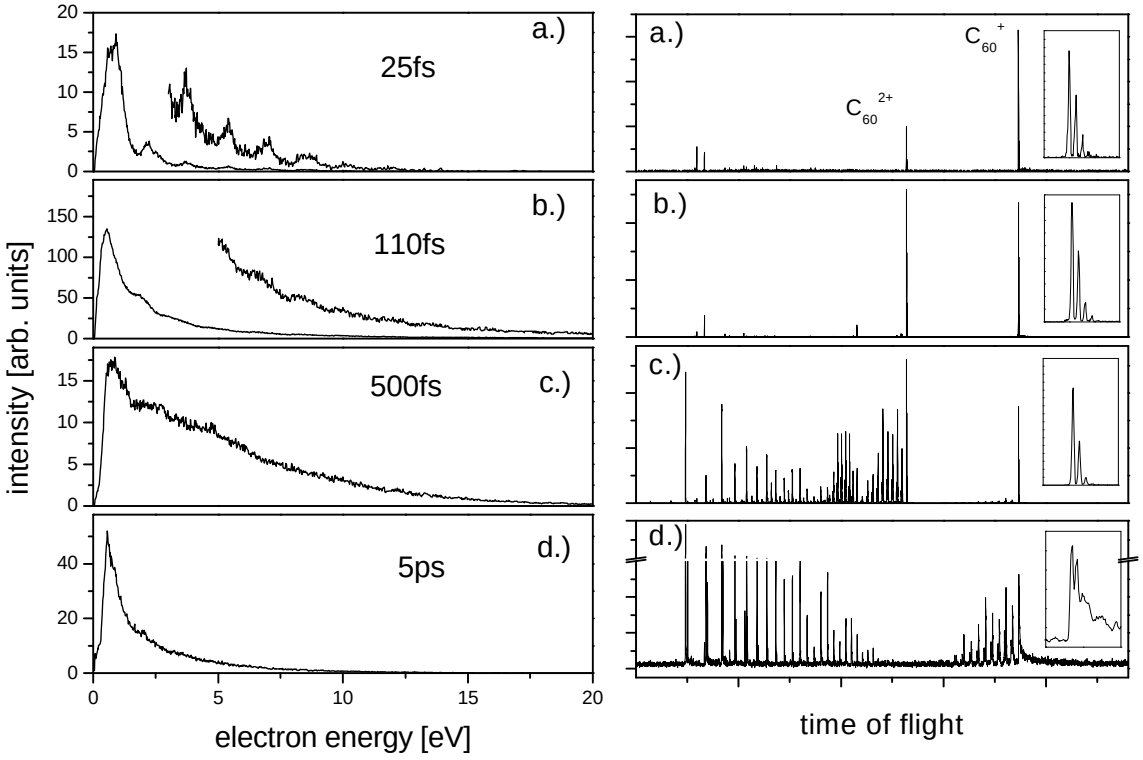


Figure 5.2: *Pulse duration dependence on photoelectron (left) and photoion spectra (right) (adapted from [CHH00]). a.)-c.) 8*10$^{13}$ W/cm$^2$ and d.) 5*10$^{12}$ W/cm$^2$. The inset shows the $C_{60}$ mass peak in detail, and indicates the onset of delayed ionization for longer pulse durations.*

fragments is produced (Fig. 5.2d, right).

The variation of pulse duration of single laser pulses exciting $C_{60}$ indicate the timescales of energy redistribution. However, the system is not allowed to relax in a field free environment, which may result in higher charge states (rather than fragmentation), more (or less) efficient energy absorption, and/or different relaxation pathways. Another technique to monitor energy redistribution is time resolved pump-probe spectroscopy. This technique is particularly useful to monitor the non-equilibrium dynamics. Curiously, only three pump-probe measurements have been made with fs-laser pulses on isolated $C_{60}$ [HCF94], [BGe97], and [Hof00]; and all of these works report solely on the $C_{60}^{+}$ yield. The results are shown in Fig. 5.3.

In each pump-probe spectrum, the $C_{60}^{+}$ yield is plotted versus time delay between two pulses of the same wavelength and duration. In the earliest work, Hohmann et al., measured one color pump-probe spectra at 620 nm. The result is presented in

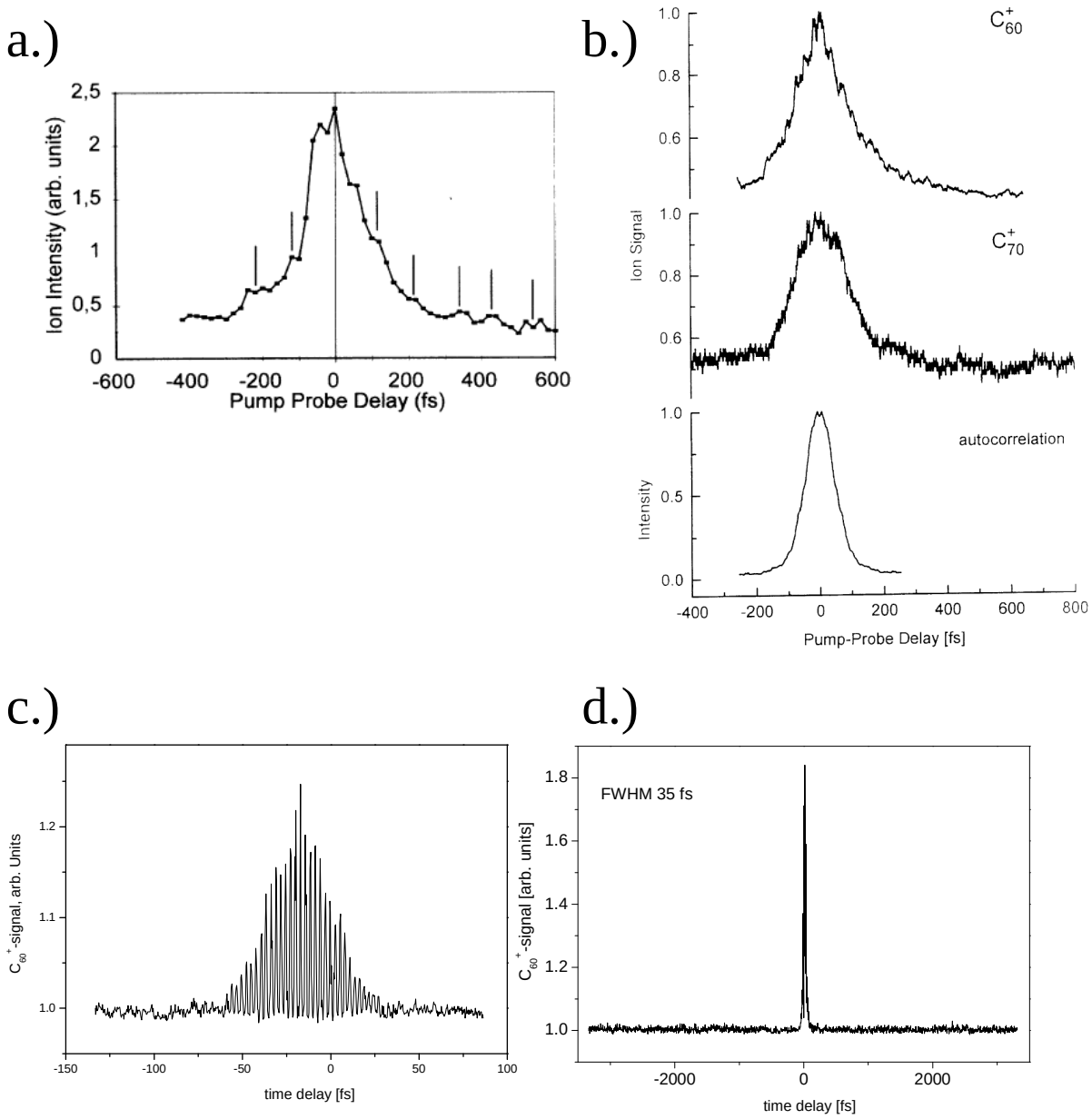


Figure 5.3: *Previous pump-probe measurements of $C_{60}$ a.) taken from [HCF94], one color (620 nm)b.) taken from [BGe97], one color (620 nm) c.) and d.) taken from [Hof00], one color(800 nm)*

Fig. 5.3a. The authors observe an oscillatory structure in the $C_{60}^+$ yield which was interpreted as an induced excitation of the Jahn-Teller active $h_g$ mode in the $^1T_{1g}$-$^1a_g$ dipole forbidden transition. A Fourier transform of the spectrum results in a frequency of 311 $cm^{-1}\pm$ 24 $cm^{-1}$, which is in agreement with the electronic ground state frequency of the $h_g(8)$ mode of 273 $cm^{-1}$. Although laser pulse intensities were not given in the paper, the authors claim that one photon saturates the $^1T_{1g}$-$^1A_g$ transition and a further 3 photons ionize $C_{60}$ (based on the intensity dependence of the yield).

In the second work, Baumert and Gerber [BGe97] have performed one color pump-probe spectroscopy at 620 nm (again no intensities were mentioned). The $C_{60}^+$ yield they recorded (Fig. 5.3b) contradicted [HCF94] in two ways. First, no oscillation of 110 fs period was found, but rather a 30 fs oscillation. Secondly, the $C_{60}$ transient could be fit by a double exponential with time constants 100 $\pm$ 20 fs and 3.0 $\pm$ 0.5 ps, which shows that the resonant intermediate is important in the excitation process. No interpretation of the oscillation was presented, however it is unlikely to have any physical meaning, as the pulse duration is significantly longer.

In the most recent work, Hoffmann measured one color (800 nm) pump-probe spectra, as is shown in Fig. 5.3c and d. In Fig. 5.3c, the $C_{60}^+$ yield for very short delay times is shown for laser intensities of $2.5*10^{13}$ W/$cm^2$ (both pulses). The oscillatory structure results from the interference pattern of the overlapping pulses. Data for a second intensity ($5*10^{13}$ W/$cm^2$) is presented [Hof00], however, the results are similar. In Fig. 5.3d, the $C_{60}^+$ transient is shown for extended delay times. The intensity was $3*10^{14}$ W/$cm^2$. No evidence of vibrational mode excitation as in [HCF94] or [BGe97] is observed. The results show only the intensity overlap of two pulses. Two reasons that no enhancement was observed are speculated [Hof00]. First, the ionization probability of the excited $C_{60}$ is small in comparison to that of $C_{60}$ in the ground state. Secondly, the number of excited molecules is small in comparison to those not excited or already ionized. Further reasons why no pump-probe dependence was measured are that the intensities were quite high and the wavelength was not resonant with lower excited states. The intensities were close to the saturation level of the $C_{60}$ yield. Additionally, the ionization regime changes from multi-photon ionization (MPI) to above barrier ionization (ABI) near the intensities used. A change of regimes could mask pump-probe effects resulting from resonant states.

No results have been published on the transient yields of fragments or of higher charges after excitation with fs laser irradiation. Of particular interest to this work

is the fragmentation channel. Transients of various fragments or fragment groups could clarify energy redistribution on the fs time scale, as well as help elucidate the fragmentation dynamics. Recent theoretical work presented evidence of an ultrafast fragmentation channel after excitation with fs laser irradiation [TNE01][JGA02]. It was predicted that the laser field efficiently excites the $A_g(1)$ vibrational mode accompanied with fragmentation occurring on a sub-ps time scale.

B. Torralva, et al. [TNE01] use a combination of tight-binding electron dynamics and a density-functional-based tight-binding approach to simulate the laser-matter interaction. With a 10-fs laser pulse of 2.0 eV photon energy, they found that for a low fluence (0.006 J/cm$^2$) the Ag(1) and the Ag(2) vibrational modes were excited. As the fluence was increased, the $C_{60}$ molecule began to fragment. The threshold fluence producing fragmentation within 1 ps was 0.117 J/cm$^2$. This corresponds to an intensity of $I_{laser} = 1 * 10^{13}$ W/cm$^2$, an intensity that can be experimentally easily achieved.

Jeschke et al [JGA02] used a different theoretical model. They considered the tight binding energy levels with time-dependent fractional occupation numbers. They observed for a laser pulse of 80 fs duration, which deposits 3.5 eV/atom energy into the system, that the cage is torn open at 90 fs after the pulse maximum and begins to emit fragments at 140 fs. These recent theoretical results, coupled with the lack of pump-probe experiments on $C_{60}$ , motivate the pump-probe experiments described in this work.

## 5.2 Experimental Observations and Discussion

Photo-fragmentation of $C_{60}$, although well understood for ns laser interaction through statistical processes, may occur through different processes under femtosecond irradiation. This work studies the fragmentation after femtosecond laser irradiation by monitoring the fragmentation dynamics experimentally. Although actual detection of fragments occurs in a TOF - mass spectrometer on a microsecond time scale, direct changes of fragmentation patterns or yields can be observed with time resolved pump-probe measurements of a fs time resolution. The results from pump-probe experiments are explored in the first section. In the second section, measurements of the spatial distribution of fragments with a position sensitive detector are described.

### 5.2.1 Ultrafast Fragmentation of $C_{60}$ : Small Fragments

The study of fragmentation with femtosecond pulses has been made primarily through single pulse excitation [HCF94, CHH00, Hof00]. The single pulse generates both the ionization and fragmentation processes. By implementing the pump-probe technique, the fs and ps time scales will be probed. These time scales push the limits of statistical models. The goal of these pump probe measurements is to investigate the possibility of non-thermal fragmentation of $C_{60}^+$.

#### One-Color Time-Resolved Pump-Probe Spectroscopy

First, single color pump-probe spectroscopy will be used to examine the fragmentation of $C_{60}$. Dissimilar pulse intensities were used for the pump and probe pulses to create an asymmetry in the pump-probe signal. For comparison, mass spectra recorded after interaction with a 50 fs laser pulse of central wavelength 800 nm at two different intensities are shown in Fig. 5.4a and b (not pump-probe).

The spectra show the ion yield versus the TOF, converted to the mass to charge ratio. These spectra are comparable for such short pulse durations with those measured previously [CHH00, CHR01]. The higher intensity mass spectrum Fig. 5.4a shows significant fragmentation, as evidenced by the large fragments $C_{60-2n}^{z+}$ for $z =$ 2 and 3, however very few small carbon clusters, $C_n^+$ for $n = 1$ to 6, are detected.

The 50 fs pulse duration is short in comparison to the electron-phonon coupling time. Since no delayed ionization has been detected for pulse durations shorter than 100 fs [CHH01], it is assumed here that all ionization occurs before fragmentation (or until a second pulse interacts with the fragment). After the final charge state is reached, the most favorable fragmentation is dependent on the internal energy. For internal energies up to 80 eV, the fragmentation is expected to proceed via neutral $C_2$ loss [Cam03]. Small charged fragments are not detected because their IP is higher than that of the heavier fragments. A higher ionization potential of small fragments means that the valence electron(s) are more tightly bound and more likely to remain on that fragment in the dissociation event. The small fragments have ionization potentials around 10-12 eV [RZE93], in comparison to the 7.6 eV of $C_{60}$.

The peaks present at m/z $< 100$ for the single pulse excitation are attributed to $H_2O^+$ and $C_3H_6O^+$ (acetone). The lower intensity mass spectrum, Fig. 5.4b, is composed of primarily $C_{60}^{z+}$ for z = 1 and 2. Little to no fragmentation is observed.

The two pulses producing the mass spectra presented in Fig. 5.4a.) and b.) were

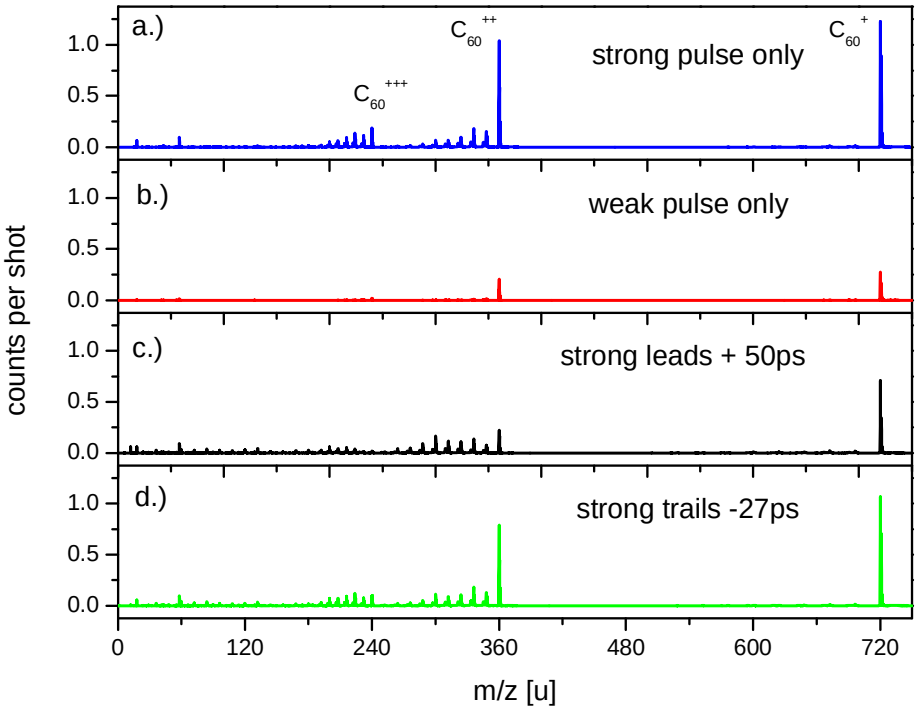


Figure 5.4: *Pump-Probe mass spectra excited with 50 fs laser pulses at 800 nm of a.) only 5*10$^{13}$ W/cm$^2$ and b.) only 1.8*10$^{13}$ W/cm$^2$ c.)pump-probe strong leads weak by 50ps and d.) strong trails weak by 27ps.*

used in a one color pump-probe measurement. As both pulses generate multiple ionization, the "pump-probe" notation indicates only which pulse interacts first. A comparison of the single pulse mass spectra with mass spectra of two different time delays where the pump pulse is interchanged is presented in Fig. 5.4 c.) and d.).

Fig. 5.4d shows the resulting mass spectra when the weaker pulse leads by 27 ps. In comparison to Fig. 5.4a, $C_{60}^{2+}$ and $C_{60}^{3+}$ are slightly reduced in intensity, which is mirrored by a slight increase in the fragments $C_{60-2n}{}^{z+}$. Trace amounts of charged light fragments are detected.

When the strong pulse leads the weak by 50 ps, as is shown in Fig. 5.4c, there is a strong decrease of $C_{60}^{z+}$ (z = 1, 2, 3) as compared to Fig. 5.4a. The yield of $C_{60}^{3+}$ and $C_{60-2n}^{3+}$ are nearly completely suppressed. $C_{60-2n}^{+}$ and $C_{60-2n}^{2+}$ undergo slight increases in yield. $C_{60}^{+}$ and $C_{60}^{2+}$ although reduced in intensity with respect to Fig. 5.4a, remain above their respective yield in Fig. 5.4b. A significant increase in the small fragments is observed. In Fig. 5.4 it is seen that the signal of the heavy fragments and ions dominate the mass spectra for each condition. The small fragments, when present,

are only a small portion of the signal.

A closer look at the small carbon clusters $C_n^+$ from the pump-probe exitation is shown in Fig. 5.5 for n = 1 to 6. Both pump-probe spectra show a dramatic increase of $C_n^+$, from n= 1 to 13 (the carbon clusters of n = 7 to 13 are not shown). Additionally, the $C_1^+$ and $C_2^+$ fragments show a strong dependence (and to a lesser degree $C_3^+$ and $C_4^+$) on the temporal order of laser pulse interaction. The peaks between the small carbon fragments are attributed to doubly charged small fragments. It is also interesting to note that the width of the small carbon fragments mass peak is significantly broader than the width of adjacent background mass peaks, indicating a kinetic energy release upon fragmentation.

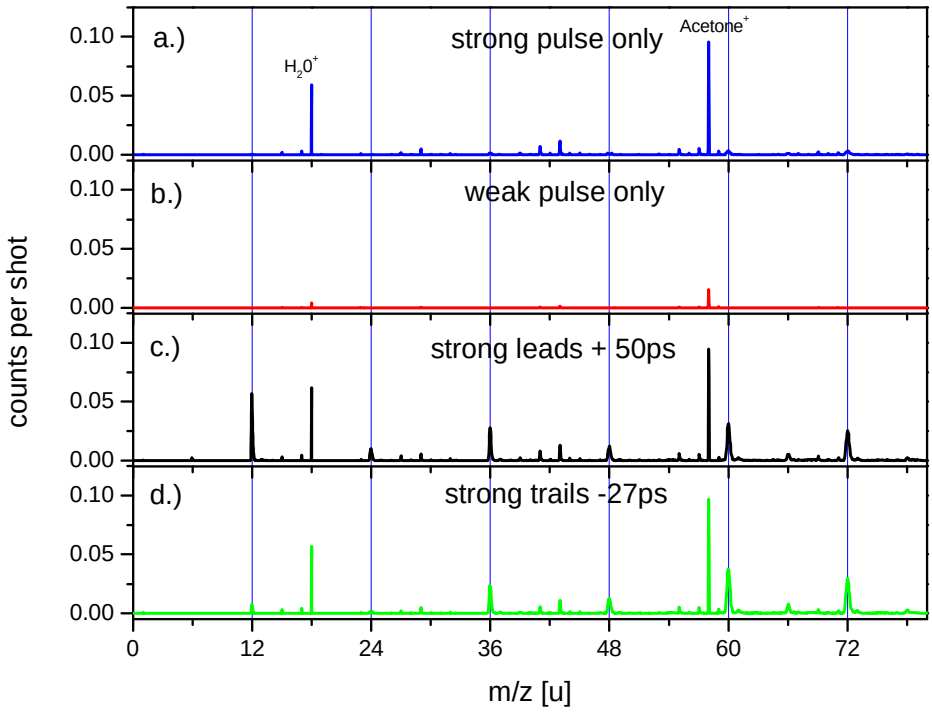


Figure 5.5: *Pump-probe dependence of the small fragments for single pulses, a.) and b.), and for pump-probe excitation, c.) and d.), This is an excerpt of the mass spectra shown in Fig. 5.4.*

A study of the yields of ions and fragments as a function of time delay between two pulses has been performed. The two replica pulses were generated in a Michelson-Morley interferometer. One pulse could be delayed arbitrarily with a translation stage. The other pulse was attenuated using a $\lambda/2$ plate and thin film polarizer. The two beams were collinearly aligned through the mass spectrometer. Measurements

were made with 2 ps resolution, scanning up to 100 ps delay. The stronger pulse interacts with the $C_{60}$ molecule before the weaker pulse at positive time delays.

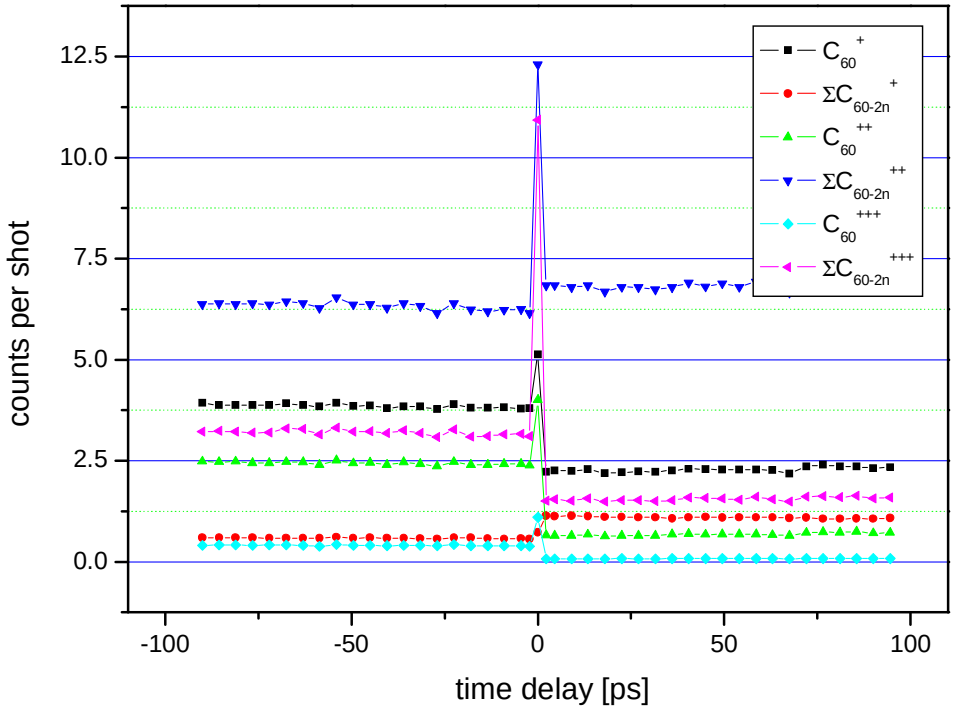


Figure 5.6: *One color time resolved pump-probe transients of* $C_{60}^{+}$ , $C_{60-2n}^{+}$ , $C_{60}^{2+}$ , $C_{60-2n}^{2+}$ , $C_{60}^{3+}$ , *and* $C_{60-2n}^{3+}$ *for laser pulses of 50 fs pulse duration, central wavelength 800 nm, and intensities* $5*10^{13}$ *W/cm*$^2$ *and* $1.8*10^{13}$ *W/cm*$^2$.

The yield of the heavy fragments ($C_{60-2n}^{+}$ , $C_{60-2n}^{2+}$ , and $C_{60-2n}^{3+}$ ) changes with interchanging pulse order, however, no dynamics were observed, as shown in Fig. 5.6. The y-axis displays the number of counts per shot, the x-axis displays the time delay between pump and probe pulses. These curves were acquired using laser pulse intensities of $5*10^{13}$ W/cm$^2$ and $1.8*10^{13}$ W/cm$^2$. The peak at zero time delay indicates the overlap of the two pulses. The increase is due to the constructive interference of the two pulses. A decrease in yield for positive delay times is observed for each of the traces, except for $C_{60-2n}^{+}$ and $C_{60-2n}^{2+}$. In other words, the amount of fragmentation to produce fullerene-like fragments increases when the more intense pulse leads.

The small fragments however show a very active pump-probe transient on the picosecond time scale as shown in Fig. 5.7. The transients of the small fragments ($C_1^+$ to $C_4^+$) are plotted as a function of time delay. For the intensities $5*10^{13}$ W/cm$^2$ and $1.8*10^{13}$ W/cm$^2$ used for the transient spectra in Fig. 5.7, the following observations

are made: the pump-probe yield of small fragments is significantly larger (at least one order of magnitude) than the yield from only the strong pulse regardless of the temporal order of pulses. The ion yields resulting from excitation with only a single strong pulse are the straight lines near zero counts per shot ($C^+$ and $C_2^+$ are the lower two lines and $C_3^+$ and $C_4^+$ are the upper two lines). For these intensities, $C_1^+$ and $C_2^+$, and $C_3^+$ exhibit increases in yield for positive time delays, while $C_4^+$ exhibits a slight decrease in yield at positive time values. The increase in yield of $C_1^+$ at positive time delays is one order of magnitude larger than the yield at negative delays. The increase of yield for $C_2^+$ is approximately 5 times greater. The pump-probe yields of these small fragments are intensity dependent, as is shown in Fig. 5.8.

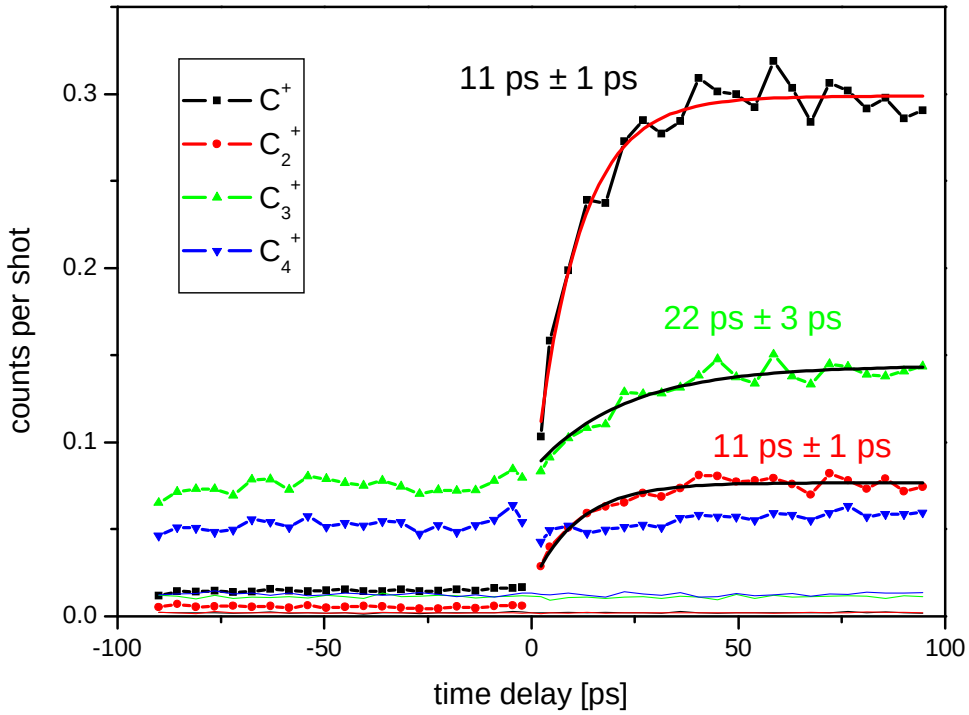


Figure 5.7: *One color time resolved pump-probe traces of $C^+$, $C_2^+$, $C_3^+$, and $C_4^+$ for excitation with 50 fs laser pulses of wavelength 800 nm and intensities of $5*10^{13}$ W/cm$^2$ and $1.8*10^{13}$ W/cm$^2$.*

Each graph in Fig. 5.8 shows the transients of four fragments at five different weak pulse intensities. The strong pulse was constant at $5*10^{13}$ W/cm$^2$. The plots furthermore contain the ion signal when only the strong laser pulse interacts with $C_{60}$. The transient signals for one given intensity were recorded simultaneously.

The $C_1^+$ transients show similar trends for different intensities. For negative time

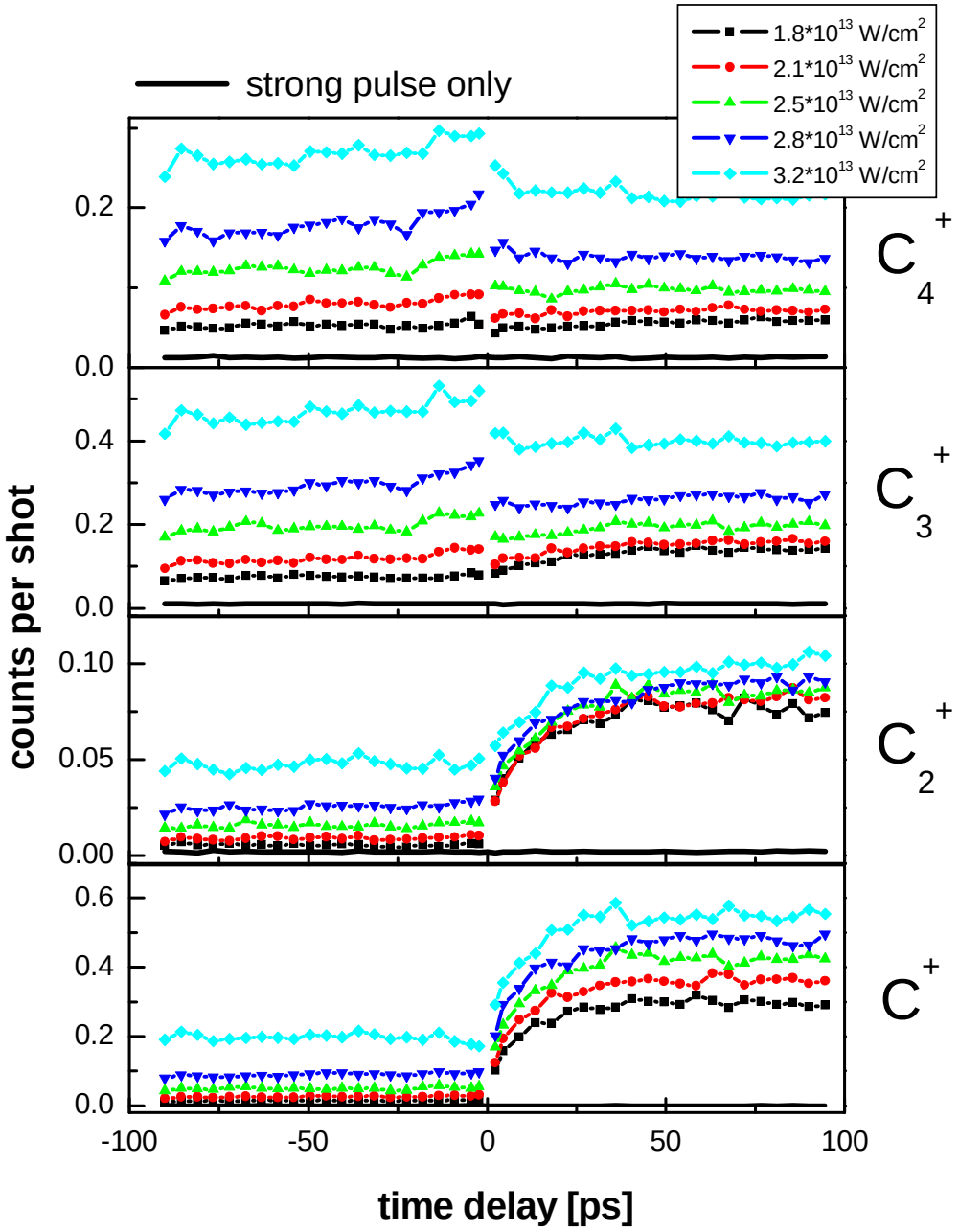


Figure 5.8: *Intensity dependence of weaker pulse on the small fragment yield of* $C^+$, $C_2^+$, $C_3^+$, *and* $C_4^+$. *The strong pulse remained constant at* $5*10^{13}$ $W/cm^2$.

delays, the transient is a flat line, while the positive time delays can be fit by a single exponential with a time constant of 11 ps ± 1 ps, as is shown in Fig. 5.7. The time constant does not change with probe intensity within the fit error as shown in Fig. 5.9a.

Analysis of the ion yield versus the laser intensity of the weak pulse shows the yield for negative time delays, when plotted on a log Signal vs log Intensity graph (Fig. 5.9b), increases linearly. For positive time delays, the yield changes with intensity linearly but with a much smaller slope. A larger slope may be indicative of a higher order multi-photon process.

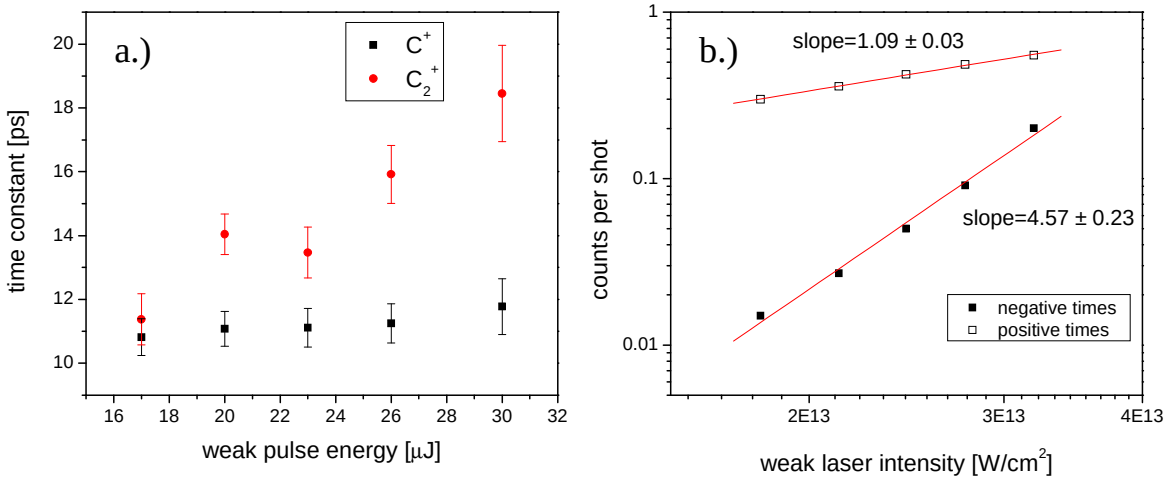


Figure 5.9: *Evaluation of the weak intensity dependence of one color pump-probe spectra. a.) time constants for $C^+$ and $C_2^+$ b.) yield dependence of $C^+$*

The $C_2^+$ transient is similar to that of $C_1^+$, a flat line for negative time delays and an exponential rise at positive time delays. However, the exponential rise in yield for positive times is slower and increases with increasing probe pulse intensity. Starting with a time constant of 11 ps ± 1 ps, the time constant increases up to 18.5 ps ± 1.5 ps.

The $C_3^+$ and $C_4^+$ yields are also probe intensity dependent. $C_3^+$ demonstrates a transition between exponential increase for weak intensities to a decrease (in comparison to negative times) in yield for higher intensities (Fig. 5.8). No exponential increase for the $C_4^+$ yield is evident. For lower intensities, the yield level remains constant for positive and negative time delays. For higher intensities, the yield is reduced from that of the negative time delays.

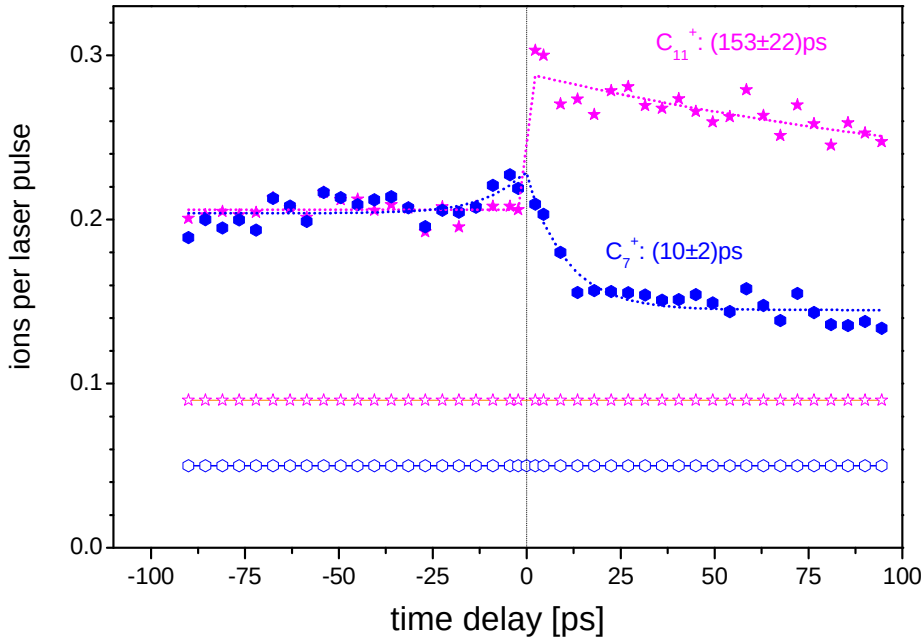


Figure 5.10: *The time dependence is shown for $C_7^+$ and $C_{11}^+$ for an excitation with 50 fs laser pulses of wavelength 800 nm and intensities of 5*10$^{13}$ W/cm$^2$ and 1.8*10$^{13}$ W/cm$^2$. (same conditions as in Fig. 5.7). The hollow symbols represent the yield level with only the stronger of the two pulses.*

One group of fragments shows a decrease in yield in the time region studied, namely the middle sized carbon fragments, i.e. $C_n^+$ for $n = 7$ to 11. Fig. 5.10 shows the time dynamic for $C_7^+$ and $C_{11}^+$. $C_7^+$ decays with a time constant of 10 ± 2 ps and $C_{11}^+$ decays with a time constant of 153 ± 22 ps.

### One-color Pump-probe Summary

One-color time-resolved pump-probe spectroscopy illuminates many interesting details about the fragmentation of $C_{60}$.

The order of interaction of a strong and weak pulse has a clear effect on all fragmentation channels of $C_{60}$. For negative time delays, the weaker pulse interacts with the $C_{60}$ molecule first and generates no fragmentation (Fig. 5.4b). The stronger pulse then interacts with the products (primarily excited $C_{60}^+$ and $C_{60}^{2+}$) initiating fragmentation and further ionization. By increasing the weak pulse intensity, the small fragment yield shows a strong intensity dependence (Fig. 5.9), indicating that the weak pulse is preparing the system for generation of small fragments, but not

actually producing any fragmentation itself. No pump-probe dynamics are observed on the negative time scales for weaker intensities.

For positive time delays, the strong pump pulse generates significant fragmentation. The weak pulse then puts more energy into the system and enhances the fragmentation yield of $C^+_{60-2n}$ . The small fragments show significant enhancement on the picosecond time scale. As the weak pulse intensity is increased, the additional energy input in the system further increases the amount of fragmentation. The decay of $C^+_4$ (and larger fragments) yield compared to negative time delays indicate an additional fragmentation of $C^+_n$, which would have been stable without further excitation. The fragmentation process leads to ever smaller fragments toward the final product of the chain, $C^+$.

Time dynamics are observed for $C^+$, $C^+_2$, and $C^+_3$ (with lower weak pulse intensity). The fragment yield exponentially increases on a 10-20 ps time scale, after which a saturation is reached, and the fragment yield remains constant up to the longest delay used in the present work, 100 ps. For the heavy fragments ($C^+_{60-2n}$, $C^{2+}_{60-2n}$, and $C^{3+}_{60-2n}$) and mother ions ($C^+_{60}$, $C^{2+}_{60}$, and $C^{3+}_{60}$) the time dynamic is a step function, on the 2 ps time resolution used in the present measurements, therefore change of yield occurs on a faster time scale.

There are several possible mechanisms to explain the observed production of small fragments. An introduction to these mechanisms will be presented here before going deeper into the experimental work. In this work, ionization is assumed to take place immediately, thus fragmentation always proceeds through the ionic state. The three possible processes are unimolecular dissociation (either statistical or non-statistical), fission (where each fragment is charged), and multiple fragmentation. The possible paths for production of small fragments are shown in Fig. 5.11, Fig. 5.12, and Fig. 5.13.

### Unimolecular Dissociation : $C_2$ loss

Unimolecular dissociation is the decomposition of a single isolated molecule into two products and can be written as

$$C^{z+*}_{60} \Rightarrow C^{z+*}_{60-n} + C_n \tag{5.1}$$

where z is 1 to 3 and n is the number of atoms lost. The (*) indicates an internally hot system. For this mechanism, the pump pulse excites the system, from which unimolecular dissociation will proceed via neutral $C_n$ loss ($n$ is exclusively 2 for the

fullerenes of low internal energy and in the case of multiple fragmentation at high internal energy $n$ can be any integer) until the probe pulse interaction. Upon irradiation by the probe pulse, further excitation and/or ionization of the charged particle and ionization of the neutral particle are possible. A schematic of this process is shown in Fig. 5.11.

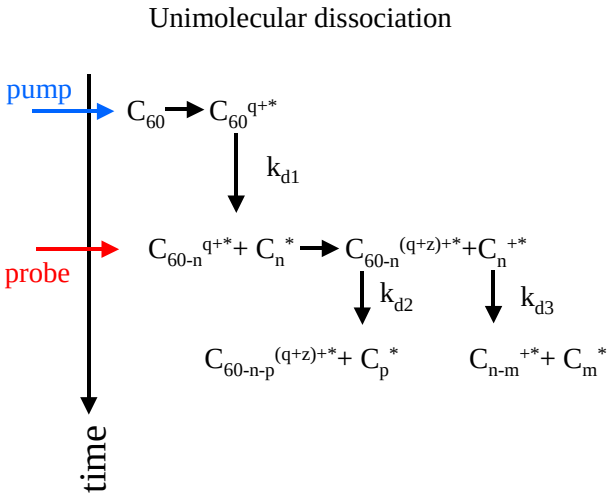


Figure 5.11: *Schematic of unimolecular dissociation and its relation to pump-probe measurements.*

This could explain the time dependent rise of small fragments observed for positive time delays, since the signal is the integral of particles ionized in the interaction volume. With increasing delay time, the amount of small fragments present in the interaction region will increase.

For unimolecular fragmentation through $C_2$ loss to be a possibility, the following two criteria must be met. First, and most critically, the rate of fragmentation (for at least one step) must be on the order of 10 picoseconds. Secondly, the neutral particle must remain in the interaction volume and be isolated from its parent. For example, a neutral $C_2$ fragment emitted immediately after the laser interaction with 1 eV of kinetic energy (this value is measured in Section 5.2.3 and is significantly above the average kinetic energy release of 0.394 eV [GME04a]) would travel approximately 28 nm in 10 ps, significantly separated from the parent however still within the $\mu$m laser focus, thus satisfying both criteria.

The first criterion can be checked through statistical models of the fragmentation process. The rate of neutral fragmentation can be roughly estimated through the

Ramsperger, Rice, and Kassel (RRK) model. The energy necessary for $C_2$ emission from $C_{60}$ in 12 ps (the fit time constant) was calculated. The critical equation is

$$k(E^*) = \widetilde{\nu}(\frac{E^* - D}{E^*})^{s-1} \tag{5.2}$$

where $E^*$ is the internal energy, $D$ is the dissociation energy, $\widetilde{\nu}$ is the average frequency, $s$ is the number of vibrational degrees of freedom, and $k$ is the rate constant. For the fragmentation step $C_{60} \Rightarrow C_{58} + C_2$, the dissociation energy is 10.8 eV [TAH03] and $\widetilde{\nu}$ is 2.9*$10^{13}$ Hz [FLS93]. The number of degrees of freedom for $C_{60}$ is 174. With Eq. 5.2, an internal energy of 300 eV is needed to produce a time constant for fragmentation of 12 ps. This is an unrealistic amount of internal energy, however, for a more realistic internal energy of 100 eV, the time constant is 3.2 $\mu$s. The observed picosecond fragmentation obviously does not correspond to the simply purely statistical model of RRK.

However, a second method to determine the rate of fragmentation has been developed under the constructs of detailed balance [TAH03]. In the work of Tomita, et al., an Arrhenius-type formula is developed to have a rate constant dependent on the microcanonical temperature.

$$k(T) = A_d exp\left(-\frac{E_d}{k_B(T - E_d/2C)}\right) \tag{5.3}$$

where $A_d$ is the pre-exponential factor which for $C_{60}$ is 3.4x$10^{21}$ $s^{-1}$ [TAH03], $E_d$ is the activation energy, $k_B$ is the Boltzmann constant, $T$ is the microcanonical temperature before fragmentation, and $C = 0.0147$ eV/K is the heat capacity. The activation energy is equivalent to the dissociation energy when no reverse activation barrier exists, as has been found for $C_{60}$ [RHR90]. Using the dissociation energy for the process $C_{60}^+ \rightarrow C_{58}^+ + C_2$ of 10.8 eV [TAH03], a temperature of approximately 5000 K (an energy of $\sim$ 75 eV) is necessary to produce a time constant for fragmentation of approximately 10 ps.

An internal energy of 75 eV is not unreasonable for femtosecond laser excitation. Later in this chapter, the fragmentation process $C_{60}^+ \rightarrow C_{58}^+ + C_2$ was measured with position sensitive detection after femtosecond laser excitation, and was found to have an internal energy of 112 eV.

Although only the fragmentation of $C_{60}$ has thus far been considered, a comparison of the dissociation energies of $C_2$ fragments from singly charged fullerenes (see Table A.1 in Appendix A or [TAG01, GME04b]) show that the dissociation energies steadily

decrease with the fragment size. Therefore the smaller fragments are more likely to fragment with the same amount of excitation energy. Dissociation energies for multiply charged fullerenes are comparable to those of the singly charged [GME04a].

The two different statistical models bring significantly different results. It is not the purpose of this work to undertake a lengthy discussion about why or which one is the better approximation. Detailed balance (from which an Arrhenius like formula can be developed) however indicates that a statistical unimolecular dissociation on a 10 ps time scale cannot be excluded.

### Asymmetric Fission

A second possibility is asymmetric fission of highly charged, vibrationally hot systems. Fission can be defined as a process in which both fragments contain a charge.

$$C_{60}^{z+} \Rightarrow C_{60}^{(z-1)+} + C_2^+ \tag{5.4}$$

Cederquist, et al. [CJS03] have considered the asymmetric fission barriers for the process in Eq. 5.4 for z = 2 to 9 [CJS03] and have compared this process to a neutral emission of $C_2$ for charge state up to 5. For doubly charged fragments, neutral fragmentation is dominant for all intermolecular separations. Fission was found to be energetically favorable for large separations (R > 13.5 Å) for initially triply charged $C_{60}$ , however the critical distance for electron transfer is $R_c = 12.7$ Åand therefore, neutral fragmentation is still thought to dominate. For charge states greater than 4, fission dominates for all separations. In the present one-color pump-probe measurements, charge states up to $C_{60}^{4+}$ are detected with the interaction of the strong pulse, while up to $C_{60}^{3+}$ for the weaker pulses. Higher charged states may exist, but are not detected because of instability. These higher charged states would be even more likely to undergo asymmetric fission.

In the asymmetric fission model, the pump pulse excites and ionizes the neutral $C_{60}$, from which fission can proceed. The probe pulse can then further excite and/or ionize the two charged fragments. The time dependence of the small fragment yield arises since there is a energetic barrier that must be crossed.

In addition, the time scale may be a result of an enhanced fission rate for smaller fragments, i.e., sequential $C_2$ loss after the pump laser pulse produces a smaller charged particle, i.e., $C_{60}^+ \rightarrow C_{58}^+$, in which the probe pulse excites the fission reaction.

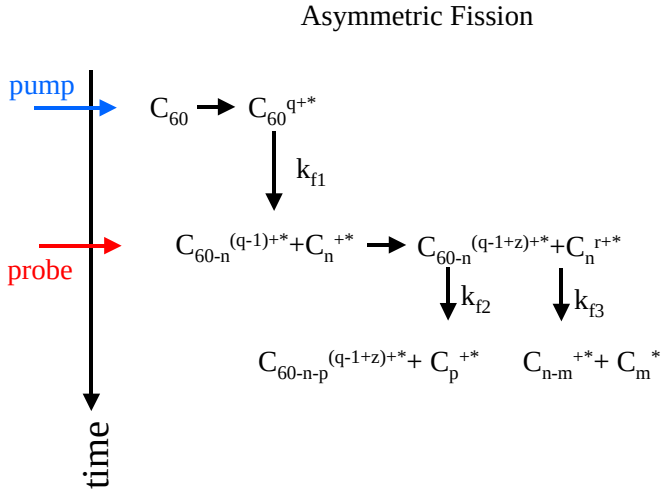


Figure 5.12: *Schematic of asymmetric fission as related to pump-probe measurements of $C_{60}$. See text for more details.*

### Multiple Fragmentation of the $C_{60}$

A third model is multiple fragmentation of the cage after extreme (>80 eV) heating of the system. In this scenario, the increase of small fragments is caused by extensive fragmentation of the cage, i.e., into 3 or more products. A time dependence can be explained when the fragmentation is dependent on an intermediate state or species. For example, Fig. 5.10 shows a decrease of $C_7^+$ yield which corresponds roughly to the increase of the small fragments, thus these medium sized fragments may be predecessors to the smaller fragments.

In the one-color pump-probe measurements, none of the models can be exclusively eliminated or favored. All three models intermix, creating very complicated fragmentation dynamics. Furthermore, the dynamic signal that is observed cannot be directly linked to a fullerene-like fragment or a smaller fragment of the already fragmented fullerene.

Nevertheless, a dynamic signal is measured on a picosecond timescale which is significantly faster than the known fragmentation times of ns-$\mu$s. A time delay of 2 ps (the shortest time delay shown) already allows for significant electronic to vibrational energy coupling since the coupling time is $\sim$ 240 fs [HHC03], thus the fragmentation discussed so far can all be explained through statistical processes. Time-resolved two-color pump-probe is performed to achieve shorter delay times, which will further

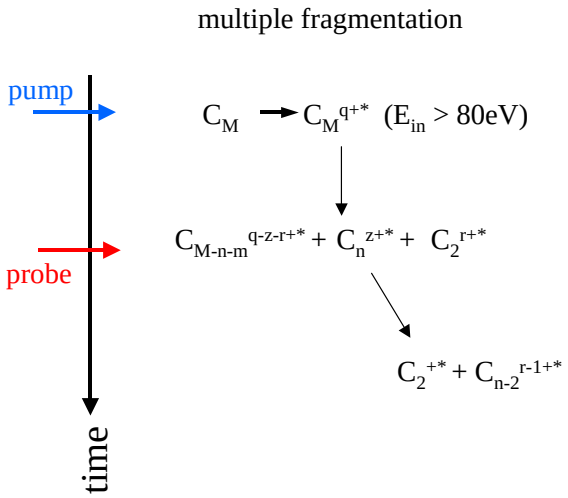


Figure 5.13: *Schematic of multiple fragmentation in relation to pump-probe measurements of $C_{60}$.*

enlighten the understanding of the fragmentation.

### Two-color Time-resolved Pump-probe Spectroscopy

In this section, fragmentation of $C_{60}$ will be investigated with two-color pump-probe spectroscopy with central wavelengths of 800 nm and 400 nm. The cross correlation as measured with the xenon ion yield was 150 fs ± 25 fs.

The two-color pump-probe measurements were performed at weaker intensities than the one color measurements, but nevertheless the dynamics of the small fragments was observed. The 400 nm pulse acts as the stronger pulse of the one color experiments, coupling sufficient amounts of energy into the system to initiate fragmentation.

A comparison of the mass spectra from the two colors measured individually and for two different pump-probe time delays is shown in Fig. 5.14. The intensities of the 800 nm and 400 nm pulses are $5*10^{12}$ W/cm$^2$ and $4*10^{12}$ W/cm$^2$, respectively. The resulting mass spectra are shown in Fig. 5.14a and b, respectively. The mass spectrum from the 800 nm pulse shows primarily $C_{60}^{+}$ and $C_{60}^{2+}$, with only trace amounts of fragmentation. The 400 nm pulse creates more fragmentation, as is expected since this wavelength resonantly couples energy into the system via the HOMO to LUMO+1 transition. Two additional mass spectra are shown for two different time delays. For

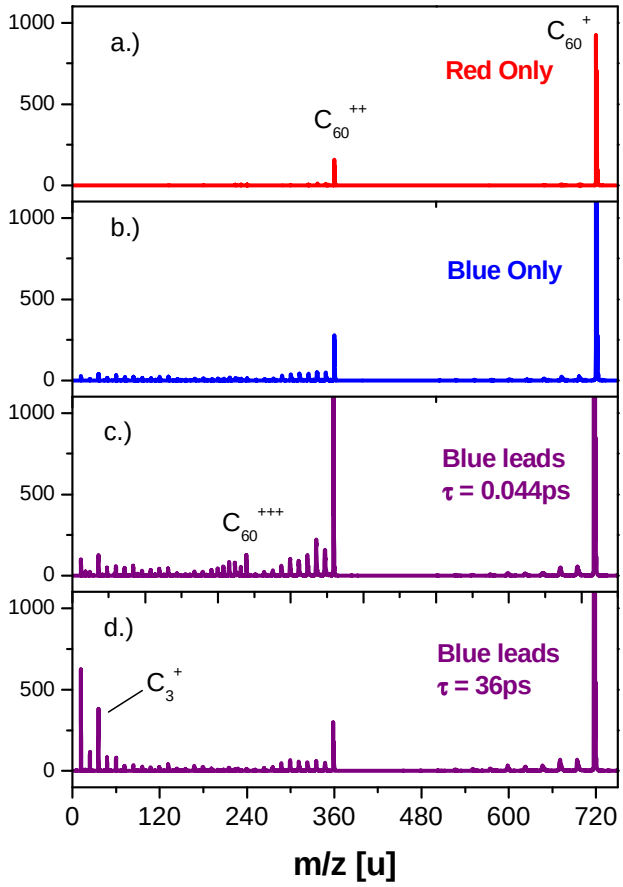


Figure 5.14: *Comparison of mass spectra taken for the two color pump-probe spectra a.) 800 nm only at 5*10$^{12}$ W/cm$^2$ b.) 400 nm only at 4*10$^{11}$ W/cm$^2$ c.) pump-probe mass spectrum for +44 fs (overlap) d.) pump-probe mass spectrum for +36ps.*

Fig. 5.14c, the two pulses are nearly completely overlapped, with the 400 nm pulse leading by 44 fs. The strong increase in signal of $C_{60}^{2+}$ and $C_{60-2n}^{2+}$ and the appearance of $C_{60}^{3+}$ and $C_{60-2n}^{3+}$ are indicative of high intensity (amount of energy per time) as both result from highly nonlinear processes. The ionization potential of $C_{60}^{2+}$ is 11.4 eV [SVK92] and $C_{60}^{3+}$ is 15.6 eV [JWP93], thus requiring the absorption of multiple photons of either 800 or 400 nm radiation to further ionize the ion. Fig. 5.14d shows the mass spectrum when the 400 nm pulse leads by 36 ps. The mass peaks generated at high laser intensity ($C_{60}^{2+}$ and $C_{60}^{3+}$) are reduced, and are similar in magnitude to those in part b.) (400 nm only). There is a significant increase in the small fragment yield, particularly for the fragments $C_1^+$, $C_2^+$, and $C_3^+$.

The two color transients of the small fragments are shown in Fig. 5.15a and b. The

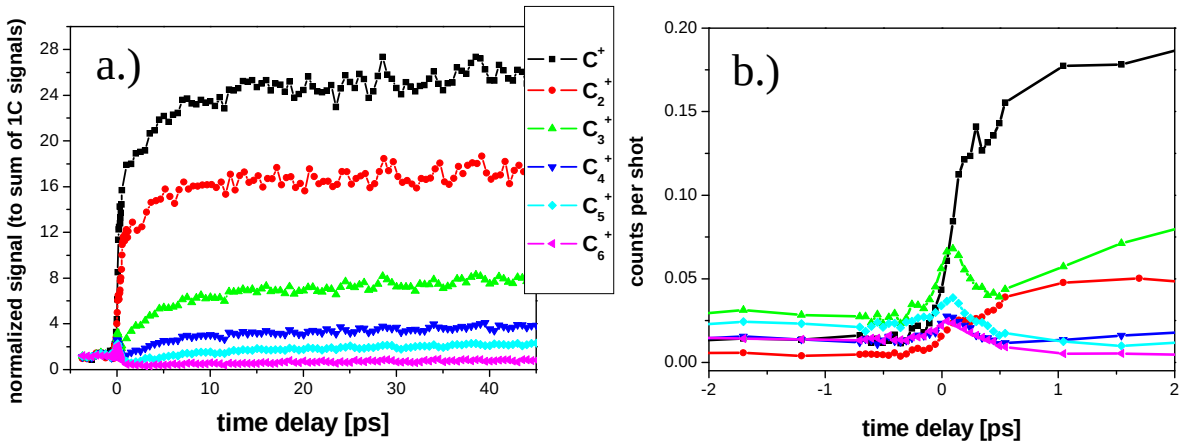


Figure 5.15: *Two color transient signals of the small fragments $C^+$ - $C_6^+$. a.) traces show up to long positive time delays b.) a closer look at short time delays for all of the fragments. The color and symbol scheme is the same for a.) and b.). The laser intensities were for 800 nm, 5*10$^{12}$ W/cm$^2$ and for 400 nm, 4*10$^{11}$ W/cm$^2$.*

traces exhibit the single pulse mass yield (measured separately) subtracted from the two-color yield and then divided by the sum of the one color yields. Mathematically, this is represented as Eq. 5.5.

$$S(t) = \frac{2C(t) - 1C(800nm)(t) - 1C(400nm)(t)}{1C(800nm)(t) + 1C(400nm)(t)} \tag{5.5}$$

This normalization shows the increase of the two-color signal over the sum of one-color signals. The zero of this normalization occurs when the 2C = 1C (800nm) + 1C (400 nm) and indicates that the yield has no two-color component. In Fig. 5.15a, the normalized signal shows that the largest increase is for $C_1^+$ and $C_2^+$, with a maximum value of 26 and 17, respectively. An extremely fast rise for these ions on the femtosecond time scale is observed, followed by a slower exponential increase on a picosecond time scale.

In Fig. 5.16, $C^+$ and $C_2^+$ were fit with double exponentials to give a first feeling of the time scales and to make a comparison with the one color results. For $C^+$, the time constants were found to be 300 fs and 6.3 ps, while for $C_2^+$, the time constants are similar at 500 fs and 6.7 ps.

A closer look at the time scale between -2 ps and 2 ps, as shown in Fig. 5.15b, displays the dynamic transient signals near zero time delay. In this graph, the transients are not normalized but rather are plotted as counts per shot. For ions $C_3^+$

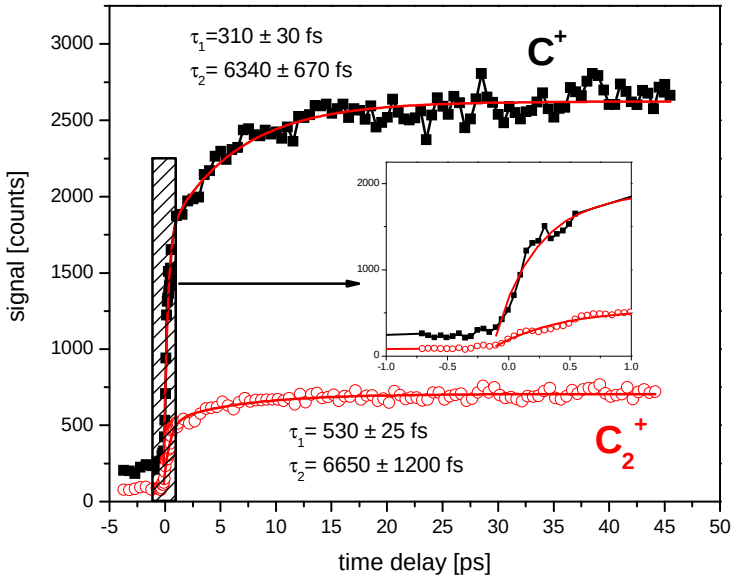


Figure 5.16: *Double exponential fit of the two color transient signals of the small fragments $C^+$ and $C_2^+$. The inset shows a close-up of the -1 to 1 ps range. The laser intensities were for 800 nm, 5*10$^{12}$ W/cm$^2$ and for 400 nm, 4*10$^{11}$ W/cm$^2$.*

and heavier, a peak at time zero is present. This is indicative of production from a very high order nonlinear processes occurring during high laser intensities. A similar increase in the small fragment yield is also observed for short pulse duration with high intensity.

For negative time delays, the relative yield of fragments is $C_3^+ > C_5^+ > C_4^+ > C_1^+ > C_2^+$ for the two color pump-probe experiment, as seen in Fig. 5.15b. The relatively high abundance of the $C_3^+$ and $C_5^+$ carbon clusters can be explained by their stability. Their binding energies are stronger than the other small carbon fragments [GMJ86]. This order is found to change for positive time delays of greater than 20ps, where $C_1^+$ and $C_3^+$ have the strongest yield of the small fragments at long delays, followed by $C_2^+$, $C_4^+$, and $C_5^+$, respectively, and as seen in Fig. 5.15a. the greatest change occurs for $C_1^+$ and $C_2^+$. It should be noted, that for the single color pump-probe measurements (Fig. 5.7), the relative abundance is found to be dependent on the weaker pulse. Only for the weakest weak pulse intensities does the $C_2^+$ fragment yield increase beyond that of $C_3^+$ or $C_4^+$.

One striking feature of the mass spectra in the small fragment region is the width of the small carbon fragments. The carbon fragment widths are significantly broader than those of the background hydrocarbons, acetone, or water (see Fig. 2.16). The

width of the carbon mass peaks is produced by the fragmentation process and is proportional to the square root of the initial KE (see Eq.2.22). The width of the peaks, particularly $C_1^+$ and $C_2^+$, have a clear dependence on time delay, as is shown in Fig. 5.17.

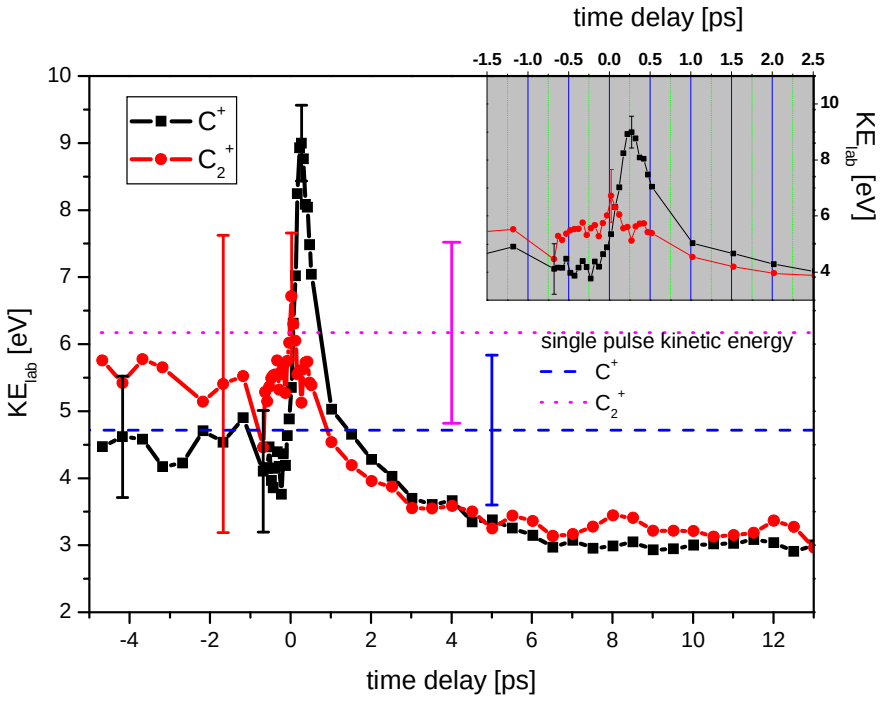


Figure 5.17: *Measured kinetic energy as a function of delay time for $C_1^+$ and $C_2^+$ for pump-probe conditions as in Fig. 5.15. For a comparison, the width of the mass peaks resulting from a single laser pulse excitation are plotted. The inset shows a blow-up of short time delays.*

The width of the mass peaks $C_1^+$ and $C_2^+$ in the TOF mass spectra were measured for each time delay. These widths were converted to kinetic energy with Eq. 2.22 [WMc55]. The calculated kinetic energy is in the laboratory frame of reference of the measured particle and is plotted as a function of time delay between pump and probe pulses in Fig. 5.17. The signal plotted is averaged over 9 measurements and the error bars indicate one standard deviation. There is a pronounced peak for short positive delay times, which decays rapidly with a 2 ps time constant. The peak of $C_1^+$ is located at +270 fs, while the peak of $C_2^+$ is at 0 fs. The exponential decay has an asymptote of the kinetic energy associated with the fragmentation by the single 400 nm pulse. For comparison, the average width resulting from a single laser pulse

excitation are shown as a dotted line ($C^+$) and dashed line ($C_2^+$). The error bars for both the single pulse and pump-probe measurements indicate one standard deviation. The width of the mass peaks corresponding to the single pulse excitation are similar to the width when the red pulse leads the blue pulse (negative time scales).

### Discussion of Two-color Pump-probe Experiments

There are several difficulties in interpretation of the two-color pump-probe results. First, the absolute number of particles created is not known. The quantitative analysis of the ion yield is hindered by the geometric collection efficiency, which, assuming an isotropic distribution, is dependent on the kinetic energy as is shown in Appendix C. For increasing kinetic energy, the probability of detection decreases because the components perpendicular to the time of flight axis are too large and the particle misses the detector. This effect is particularly critical for small fragments, such as $C_2$, which can gain significant kinetic energy in a fragmentation or fission process.

In Fig. 5.17, the laboratory frame kinetic energy was found to change between 3 and 9 eV. This corresponds to a change in collection probability between 6.6% and 2.2%, respectively, and would indicate that the increase in small fragment yield shown in Fig. 5.15 is primarily due to the increase in the number of fragments rather than the collection probability. It should be noted that the measured kinetic energies are significantly higher than those expected from statistical fragmentation of fullerene fragments, and thus, may come from different processes. For comparison, the kinetic energy release in the lab frame of $C_2$ for metastable fragmentation has been found to be 0.381 eV [GME04a] and the kinetic energy release after single pulse femtosecond excitation has been found to be 0.96 eV (calculated from $C_{58}^+$ distribution, see Fig. 5.25).

### Model 1

For a first order approximation model, the increase of kinetic energy due to Coulomb repulsion of two ions with small separation distance was considered. Under this model, the pump pulse induces ionization and fragmentation of $C_{60}$. The fragmentation occurs through neutral $C_n$ loss, with $n = 1, 2, 3, ...$ with a certain kinetic energy release (i.e. initial velocity). The probe pulse, at given time delay, ionizes the neutral fragments.

Several assumptions were made to estimate the effect of Coulomb repulsion. The most constrictive assumption is that the fragment is created at time zero, whereas the fragmentation will occur on a time scale related to the internal energy of the molecule and can extend to microseconds. A second assumption is that the charge of the smaller fragment is +1 (given from mass spectra) and the second fragment (assumed large fullerene) is +2. The charge of the larger fragment was chosen as 2 because the number of fragments appears to be greatest for doubly charged fragments (see Fig. 5.14). A third assumption is that these charges are assumed to be point charges at all time delays. The fourth assumption is that the fragment is emitted along the time-of-flight axis, either toward or away from the detector, ensuring that the particles will be incident on the detector. In a linear Wiley-McLaren time of flight apparatus, the kinetic energy is directly related to the time difference between fragments emitted with equal magnitude velocity but opposite directions.

In this model, the only fit parameter is the initial velocity, which can be determined by the asymptote of the kinetic energy at long time delays. The total kinetic energy is given by

$$E_{total}(t) = E_{k0} + \frac{1}{4\pi\epsilon_0}\frac{q_1 q_2}{(r_0 + v_i t)} \tag{5.6}$$

where $E_{k0}$ is the initial kinetic energy of $C^+$ or $C_2^+$, $q_1$ and $q_2$ are the charge of the two fragments of a fragmentation event, $r_0$ is the initial radius, $v_i$ is the initial velocity, and $t$ is the time difference between pump and probe pulses.

In Fig. 5.18, the measured experimental kinetic energy of $C^+$ (top) and $C_2^+$ (bottom) are compared to the calculated kinetic energies including an additional Coulomb repulsion. The fragment is assumed to be created at time zero at the radius r = 0.35 nm (the mean radius of $C_{60}$) with a initial kinetic energy of 2.9 eV for $C^+$ and 3.2 eV for $C_2^+$. With these kinetic energies, it is seen that the influence of the Coulomb repulsion is limited to very short time delays, i.e. the initially neutral fragment leaves the parent so quickly that when it becomes charged it is far enough away that the Coulomb energy is weak.

Further improvements to Model 1 can be made, such as an inclusion of a fragmentation distribution (in time and velocity). A second possibility for improvement is to consider a slower increase of the separation between charges. This might occur in a process similar to the strong-field charge localization model recently suggested by Markevitch, et al. [MRS04]. For $C_{60}$, however, this expansion of a molecule may be initiated by simply populating excited electronic states which are anti-bonding. This idea will be further developed in Model 2.

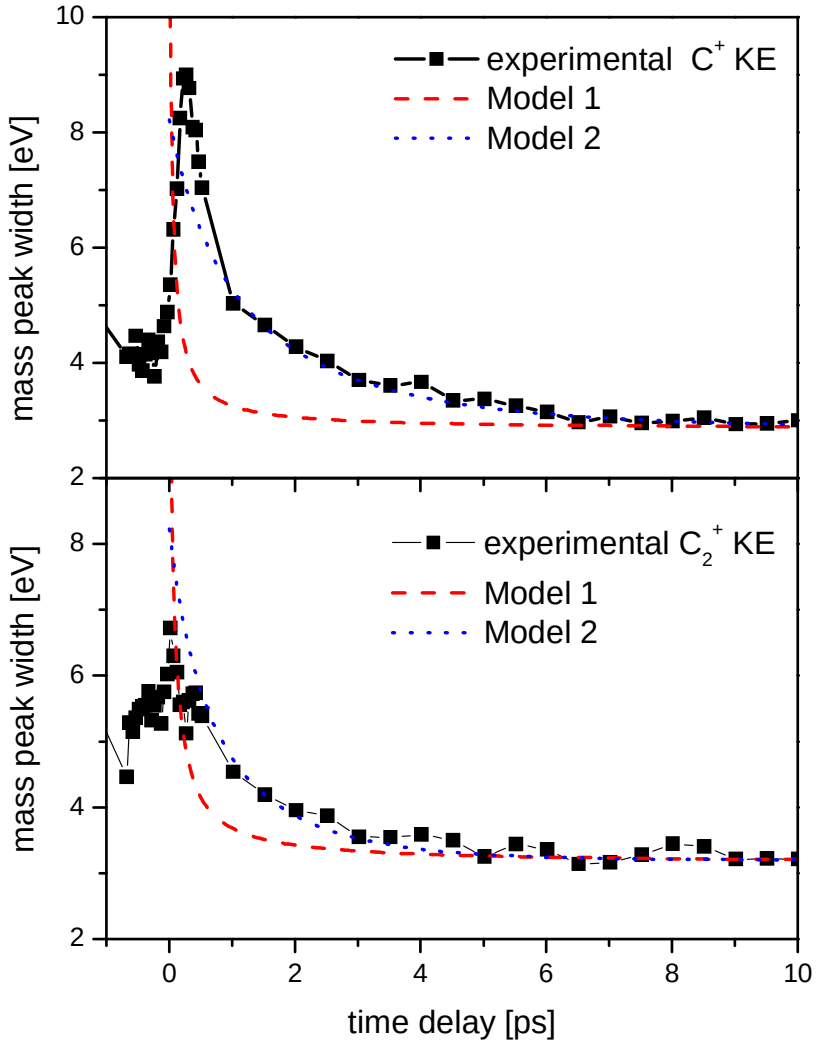


Figure 5.18: *The total kinetic energy of $C^+$ (top) and $C_2^+$ is determined for two different models. The models are compared to the measured kinetic energy of the mass peak in two color pump probe experiments when the 400 nm pulse leads the 800 nm pulse (see Fig. 5.15). The details of the two models are presented in the text.*

### Model 2

Model 2 also approaches the measured kinetic energy as an effect of the Coulomb repulsion of two charges. However, the approach is to model the apparent charge separation. The charge separation is initially set to $r_0 = 3.5$ Å and will increase exponentially out to a maximal separation. As in Model 1, the charges are assumed to be point charges of $q_2 = +1$ and $q_2 = +2$.

The total kinetic energy can be defined as

$$E_{total}(t) = \frac{1}{4\pi\epsilon_0} \frac{q_1 q_2}{(r_{M2}(t))} \tag{5.7}$$

where the time dependent separation $r_{M2}(t)$ is defined as

$$r_{M2}(t) = r_0 + r_1 \left(1 - exp\left(\frac{-t}{\tau}\right)\right) \tag{5.8}$$

with $r_0 + r_1$ the maximum possible separation and $\tau$ the time constant to reach the maximum. There are two fit parameters, $r_1$ and $\tau$. The fits were made starting with + 1 ps. The best fit was for $C^+$, $r_1 = 6.5 \pm 0.2$ Å and $\tau = 3.0 \pm 0.2$ ps and for $C_2^+$, $r_1 = 5.5 \pm$ Å and $\tau = 1.6 \pm 0.2$ ps. The results of these fits are shown in Fig. 5.18.

The maximal separation, $r_0 + r_1$, are 10 Å and 9 Å for $C^+$ and $C_2^+$, respectively. For these internuclear separations, asymmetric fission has been calculated to be energetically favorable [CJS03] for the reaction $C_{60}^{3+} \rightarrow C_{58}^{2+} + C_2^+$. However, it is pointed out that the critical distance (6.35 Å) for electron transfer is shorter and therefore neutral fragmentation is dominant. Higher charge states require that the two particles are even further separated to give the measured kinetic energies.

Should asymmetric fission be responsible for the width of the small carbon fragments, the increased width would also appear in measurements with the position sensitive detector (see Section 2.6). Although an extra width is observed with the double charged fragments, this width is thought to originate from singly charged fragments of the same m/z ratio. Thus, the high kinetic energy fragments appear ***not*** from the fullerene fragments.

The expansion of the $C_{60}$ molecule is thought to proceed upon excitation of excited electronic states. Torralva et al. [TAl01] have shown that upon the excitation of $C_{60}$ with a 12 femtosecond laser pulse, the diameter increases from 7.2 Å to 8 Å with maximal extension of nearly 9 Å. However, a direct comparison to their theoretical work is difficult, because excitation with a 12 fs laser pulse is significantly different than the excitation with a 100 fs laser pulse.

The dynamics of highly excited $C_{60}$ are extremely complicated. In the present work, it is likely that the cage is severely deformed (and possibly broken) after the first excitation pulse. It is not presently known why the time scales of $C^+$ and $C_2^+$ are different. Furthermore, the behavior of $C^+$ for short delay times ($< 1$ ps) is puzzling.

The quantitative analysis presented here only indicates that it is necessary to account for Coulomb repulsion in the interpretation of the results. In addition to the complications of KE dependent detection efficiency, the origin of the small fragments is not known. There are many pathways leading to the smaller fragments of $C_1$, $C_2$, and $C_3$ as outlined in Fig. 5.11, Fig. 5.12, and Fig. 5.13.

The results presented on the width of mass peaks were a by-product of the pump-probe measurements, and were not the sole intention of the experiment. The use of Gaussian fits is somewhat arbitrary and does not necessarily represent reality. A better way to measure the mass peak widths would be to pulse the extraction field with a given delay, allowing the particles to spread spatially, thus increasing the time-of-flight distribution.

Even though the geometric detection efficiency and the source of fragments hinders the interpretation of the results, information about the fragmentation process can be extracted. The widths of the small carbon cluster mass peaks are certainly a combination of both a kinetic energy release and Coulomb repulsion. In particular, these two-color time-resolved pump-probe measurements provide new results concerning shorter time dynamics of fragmentation of $C_{60}$ than the one-color pump-probe measurements of the previous section. The observed dynamics of small fragments are similar to the single color pump-probe, with a dramatic increase in $C^+$, $C_2^+$, and $C_3^+$ yield when the blue pulse (large intensity pulse) leads the weaker 800 nm pulse. The transients again exhibit a picosecond time constant, although these time constants are slightly shorter than the time constant found in Fig. 5.7. The difference in picosecond time constants is not completely understood at this point. The time constant will depend on the internal energy and thus the rate of fragmentation.

In addition to the picosecond time constant, a sharp increase in the ion yield of small fragments is observed on a femtosecond time scale. Additionally, the small fragments are found to have a peak in kinetic energy near time zero, which then decays on a few picosecond timescale to a value lower than the single pulse.

The ion yield and kinetic energy dynamics are not fully understood. The increase in yield has been found to be a result of both increased number of fragments or a decrease in Coulomb repulsion. Further modelling is needed to determine the relative

importance of these two possibilities. In either case, the observed dynamics must exist to explain both measurements.

The possible fragmentation processes leading to the small charged fragments are the same: sequential $C_2$ loss, fission, or multiple fragmentation of the fullerene.

### Summary of the Formation of Small Fragments

There are many pathways to reach the small charged fragments as shown in the three figures 5.11, 5.12, and 5.13, and therefore it is difficult to conclusively determine which is the dominant process. Of the three mechanisms, the processes producing directly a small charged fragment (fission or multiple fragmentation) appears to be most likely.

Neutral fragmentation with subsequent post-ionization requires multi-photon ionization of the neutral fragment. This is a highly non-linear process since the ionization potentials of small carbon fragments are on the order of 10 eV [RZE93]. If this were the dominant channel, a strong intensity dependence would be expected. The slope of $1.09 \pm 0.03$ in Fig. 5.9b indicates that the production of small fragments is not a high order process.

A further argument why neutral fragmentation is not the dominant process is that the charged small fragments are also detected for single pulse durations of high enough intensity. These fragments originating in this excitation must be released charged or undergo multiple fragmentation steps (and retaining the charge). The dissociation of fullerene-like fragments is typically through neutral $C_2$ loss. The fragmentation of carbon cluster-ions containing 25 atoms or fewer generally proceeds through emission of neutral $C_3$. Thus several fragmentation processes are required to reach either $C_2^+$ or $C_1^+$. Therefore, it seems unlikely that the fragmentation pattern of small carbon fragments that $C_1^+$ and $C_2^+$ would become dominant through sequential fragmentation steps.

Fission of $C_2^+$ from the fullerene cage is expected to be most likely for charge states greater than three [CJS03]. From the single pulse mass spectra (see Fig. 5.4a. or, to a lesser extent, Fig. 5.14b.) triply charged species exist.

A scenario in which the cage undergoes multiple fragmentation would result in small- and medium-sized charged fragments, which could then undergo further fragmentation, thus avoiding an otherwise necessary long chain of sequential evaporation of $C_2$ units. Multiple fragmentation is expected to begin at excitation energies of 80

eV [Cam03] and would also explain the larger sized fragments present in the mass spectra. Indeed a decrease in yield for $C_7^+$ is observed with a subsequent increase in $C_2^+$.

Taking these arguments into consideration, the best model for formation of the small fragments is the multiple fragmentation model. This is further backed in measurements with the position sensitive detector, where the increase of kinetic energy is not apparent for the large fullerene fragments. More discussion will follow the presentation of the position sensitive detector.

There are several reasons why the determination of one fragmentation pathway is difficult. The first is that fragmentation is always measured after the time necessary to leave the acceleration region, i.e., the femtosecond time resolution and the time of fragmentation is not completely certain because the detection time is on the order of microseconds. Thus, it is difficult to detect the difference between ultrafast fragmentation (fs) or sequential ionization or fast fragmentation (ps to $\mu$s) after ionization.

The second problem is the amount of internal energy in a particular molecule, which determines the dissipation mechanism and rate. The number of absorbed photons of $C_{60}$ molecules in a Gaussian beam is expected to have a power law distribution [MHH03]. Thus, for a particular laser energy, sequential $C_2$ loss could occur for those molecules with relatively low amount of photons absorbed (the number of $C_2$ units lost depends on the internal energy), while for other molecules, fragmentation would proceed through multiple fragmentation of the cage. The absorption distribution will also change when non-adiabatic multi-electron dynamics becomes important in the absorption of energy. For $C_{60}$ under 800 nm excitation, the onset of these dynamics is expected to be $5*10^{12}$ W/cm$^2$ (see Section 4.2.6).

A third challenge is that the femtosecond and picosecond timescales are significantly shorter than the time needed to reach equilibrium. Thus, it is not completely certain with which form of the fullerene the probe pulse interacts. Molecular dynamics calculations have been interpreted to determine the structure of $C_{60}$ for various internal temperatures [KTo94]. The structure remains intact, although "floppy" for internal temperatures up to 4000 K; at 4200 K, the $C_{60}$ cage opens and forms "pretzels", for temperatures greater than 5000 K, the then open linked chains begin to fragment. Although this calculation was for equilibrium, recent theoretical work shows that the deformation of the cage structure occurs on a few hundred femtosecond time scale. The excitation to these temperatures is not unrealistic even for a femtosecond laser

pulse of 100-150 fs duration. $C_{60}$ at these high temperature can undergo multiple fragmentation until the remaining internal energy is below the energy needed for the next fragmentation step.

The increase of ion yield of small fragments on the picosecond and femtosecond timescale challenges statistical models for fragmentation rates. The amount of internal energy necessary to produce fragmentation on the picosecond timescale is unrealistically high using simple RRK theory, however, a more sophisticated model based on detailed balance indicates that picosecond fragmentation occurs for $C_{60}$ with readily accessible amounts of internal energy.

As mentioned in Chapter 3, non-statistical fragmentation can occur in the following three cases: excitation to a dissociative state (repulsive potential energy surface), fragmentation before complete energy redistribution, or excitation of one particular vibrational mode, which leads to fragmentation. In the present experiments, only the first two cases of non-statistical fragmentation are a possibility. The excitation of one particular vibrational mode in the infrared would be achieved through impulsive stimulated Raman excitation, however, for a single laser pulse of duration 100 fs, it would not be possible to selectively excite any mode. In addition, for the pulse duration of 100 fs, both el-el coupling and some el-ph coupling have occurred further reducing the probability of the population of a single state. An excitation to a dissociative state or population of this state through non-adiabatic transitions is not directly to observed experimentally. It is necessary to consider theoretically the potential energy surfaces and even though this is a possible reaction pathway, it will not be considered further in this thesis.

Another possibility for a non-statistical process is that the fragmentation occurs before a complete energy redistribution. There is an efficient energy redistribution among electronic degrees of freedom [CHH01] and electronic to vibrational degrees of freedom [HHC03] for $C_{60}$, the femtosecond time scale for an increase of the fragmentation yield would be particularly interesting as it might indicate a direct (non-statistical) fragmentation path. Beyond the femtosecond timescale, fragmentation can be considered through statistical models.

### 5.2.2 Two-color Pump-probe : Large Fragments

It is also of interest to study the dynamic signal of large fragments of $C_{60}$. The mother ions and fullerene-like fragment pump-probe transient signals are shown in

Fig. 5.19. The y-axis is the normalized yield (as in Eq. 5.5) with respect to the sum of single pulse and is plotted versus time delay. This spectrum was measured with intensities of 7*$10^{12}$ W/cm$^2$ for 800 nm and 4*$10^{12}$ W/cm$^2$ for 400 nm. Xenon is included to display the cross correlation width and the location of time zero, where the two pulses overlap. The cross correlation width, as measured by xenon, was found to be 125 fs $\pm$ 5 fs. The right hand side of the xenon transient does not go to zero, which is caused by the underlying mass peak of $C_{11}^+$ that has the same m/z ratio as xenon. $C_{60}^{2+}$ and $C_{60-2n}^{2+}$ exhibit a strong increase in yield near the overlap of pulses, reaching 8 times (or 6 times, respectively) the yield resulting from the sum of one color signals. The maximum yield occurs 50 fs after time 0, indicating a resonant intermediate state in the excitation. This resonant state is expected to be the second lowest unoccupied molecular orbital (LUMO+1). The excitation is resonant with one photon of 400 nm (3.1eV). The ion transient peak width is also significantly broader than the cross-correlation peak.

The $C_{60}^+$ yield shows an increase that has a maximum at +50 fs. Although the signal is asymmetric, it is evident that the signal is broader than cross correlation width, which has been previously observed [HCF94][BGe97].

The singly charged fragments, $C_{60-2n}^+$ do not have a pronounced peak near the overlap of the two pulses. The integrated yield increases during the laser irradiation overlap with a maximum about 100 fs later. A slight decay trend is observed for longer time delays for the $C_{60-2n}^+$ fragments. The production of singly charged fullerene-like fragments primarily comes from the amount of energy coupled into the system. Delaying the input of probe pulse energy allows for better absorption. This may be related to the electron-phonon relaxation time, enhanced cross-section of excited states, and/or nuclear motion. Because their time-dependent signal is independent of the overlap of the two pulses, this is a particularly interesting group of fragments, which could be used for optimization experiments with temporally modulated pulse forms. Such experiments will be described in the following chapter.

Fig. 5.20a shows the influence of 800 nm intensity on the yield of $C_{60}$ at positive time delays. The intensity of the blue pulse (400 nm) was held constant at a low intensity of 3*$10^{10}$ W/cm$^2$. Plotted on a log-log graph, the yield is a linear function of intensity between 30 and 100 $\mu$J of laser energy. For energies less than 30$\mu$J, no signal was produced by the 800 nm pulse. At energies higher than 100$\mu$J, saturation occurs. For atoms, a non-resonant process results in a yield proportional to $I^n$, where $n$ is the number of photons [DKr00]. This has also been applied previously to $C_{60}$ [THD00],

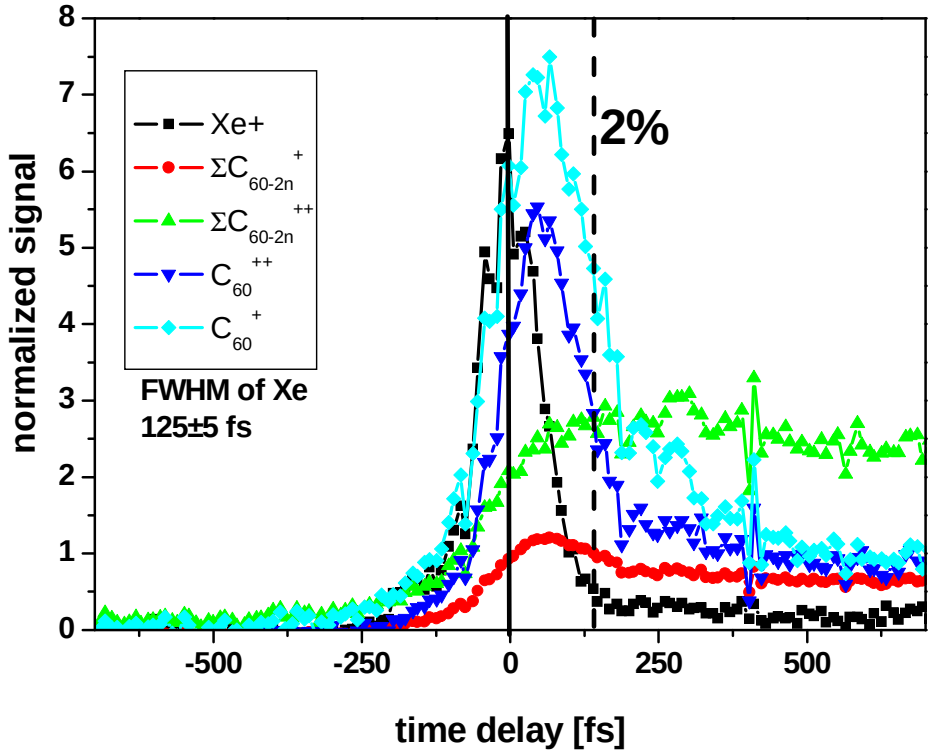


Figure 5.19: *Transients of $C_{60}^{+}$ , $C_{60}^{2+}$ , and their fragments $C_{60-2n}^{+}$ and $C_{60-2n}^{2+}$ . The mass spectra were recorded laser intensities of 7*10$^{12}$ W/cm$^2$ for 800 nm and 4*10$^{12}$ W/cm$^2$ for 400 nm. The line marked 2% indicates where the $Xe^{+}$ signal is 2% of its maximal height.*

although this interpretation has more recently been questioned [HHC03]. The slope in the present experiment is 2.75 ± 0.18. This may indicate a direct 3 photon process. The excitation of the LUMO+1 state with 3.1eV (400 nm) would place the ionization potential within 3 photons of 1.55 eV (7.58-3.1= 4.48 in comparison to 3*1.55 eV= 4.65 eV). This is a rather unlikely explanation since there are resonant states (Rydberg States) which lie between the LUMO+1 state and the IP.

The right hand side of Fig. 5.20 shows the intensity dependence of 400 nm of the $C_{60}^{+}$ transient at three points along the transients, positive times, negative times, and on the peak. The 800 nm pulse intensity was kept constant at intermediate intensity of 7*10$^{12}$ W/cm$^2$. The slopes on positive time scales and the peak are significantly below one, with the slope of the peak being slightly higher. The yield at negative time delays is not linear. For the lowest energies, there is not a significant increase of yield intensity above that of 800 nm alone.

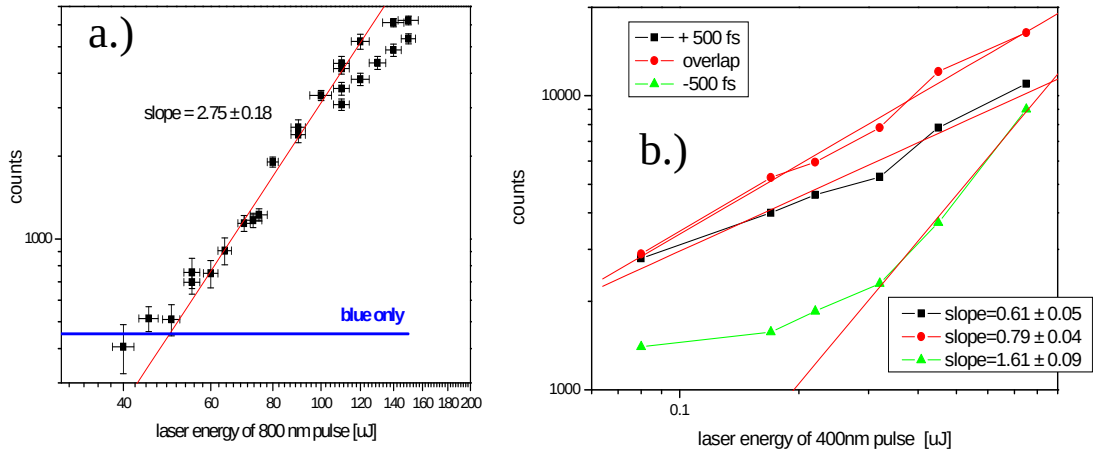


Figure 5.20: *Intensity dependence of $C_{60}^{+}$ with a) 800 nm, 400nm constant at 3*10$^{10}$ W/cm$^2$ b.) 400 nm, 800 nm constant at 7*10$^{1}$2 W/cm$^2$.*

### Summary of Large Fragments

The heavy fragments show little dynamics outside of the overlap of the two pulses. The interesting time-dependent signal of the complementary small fragments is not observed for the large fragments. This supports that the small fragments are produced in a different fragmentation event. The increase in fragmentation for positive time delays can be a result of enhanced energy absorption in the ionic state.

## 5.2.3 Position Sensitive Detection of Fragmentation

In this section, the photo-ion spectrum of $C_{60}$ after interaction with a femtosecond laser pulse has been measured with a position sensitive detector (PSD). In comparison to a traditional time-of-flight, the position sensitive detector allows for direct detection of the velocity components of ionic fragments perpendicular to the time of flight axis. The complex fragmentation pattern of $C_{60}$ provides an excellent example to learn about the capabilities of the position sensitive detector.

The first measurement with the position sensitive detector recorded the 2D image for various fragment sizes. Fig. 5.21 shows the series of fragments $C_{60-2n}^{z+}$ for n = 0 to 6 and z = 1 and 2 generated from laser interaction with a 100 fs laser pulse at 800 nm and 74 $\mu$J energy per pulse (6*10$^{12}$ W/cm$^2$). The corresponding mass spectrum is presented in Fig. 5.22. The mass spectrum indicates that the amount of

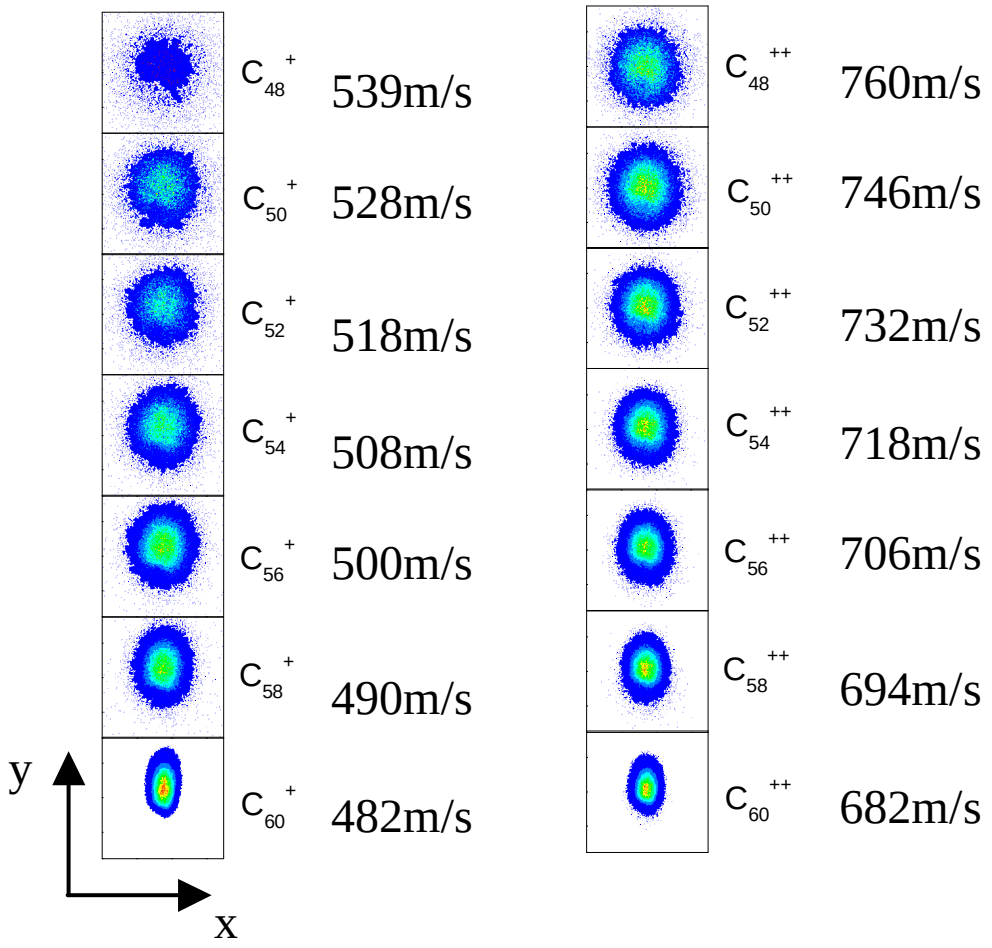


Figure 5.21: *Position sensitive detection of the photo-fragmentation of $C_{60}$ after interaction with 100 fs, 800 nm laser pulse of $6*10^{12}$ $W/cm^2$. Each x-axis and y-axis are 150 pixels long for each mass. The acceleration voltage is 500 V in this figure. The velocity corresponding to the length of the whole axis is written to the right of each plot. The contour indicates the number of counts. The absolute scale of the z-axis changes for each 2D image.*

fragmentation is small in comparison to the amount of mother ions remaining. There is a factor of 10 between the integral over $C_{58}^{+}$ (1115 counts) and $C_{60}^{+}$ (12919 counts). The doubly charged mother ion, $C_{60}^{2+}$ (3586 counts) is only 3 times greater than $C_{58}^{++}$ (1316 counts).

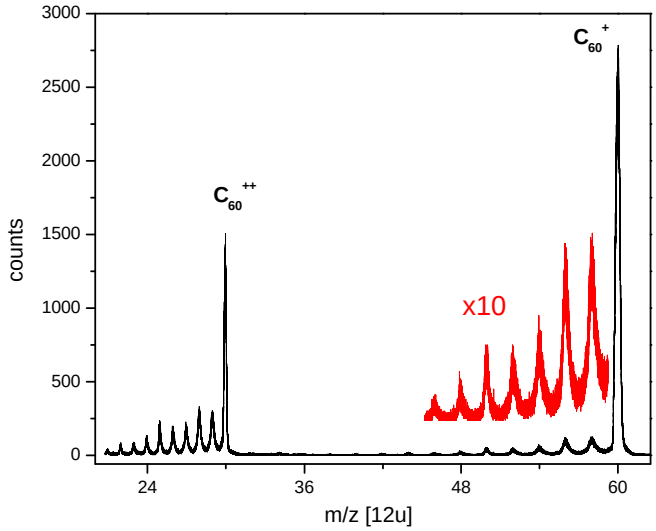


Figure 5.22: *Time of flight mass spectrum corresponding to the position sensitive detection of the photo-fragmentation of $C_{60}$ after interaction with 100 fs, 800 nm laser pulse of $6*10^{12}$ $W/cm^2$ shown in Fig. 5.21.*

The x- and y-axis in Fig. 5.21 are plotted in pixels which is directly related to the distance (each pixel is 0.25 mm). Every x- and y-axis has 150 pixels. Due to different flight times of fragments with different charge to mass ratios, the velocity which the axes represent changes as indicated in Fig. 5.21. The contour is a linear scale of the counts, with the highest number of counts in the center and decreasing with increasing radius. The absolute scale for the contour changes with fragment size.

The spatial distribution increases in both the x- and y- coordinates with decreasing fragment size (despite the decreasing flight time). Four quantities determine the size and shape of the 2D fragmentation distribution: the time-of-flight of the particle, the oven temperature, the laser beam interaction volume, and fragmentation (see experimental section for more information). The TOF of $C_{60}$ was measured to be 71.3 $\mu$s for an acceleration field of 250 V/cm. The $C_{60}^{+}$ and $C_{60}^{2+}$ spatial distributions are independent of fragmentation, and thus the spot size for these ions indicate the apparatus function and can be deconvoluted from the measured data (see Fig. 2.5 and Fig. 2.6). The ellipticity is due to the $C_{60}$ molecular beam propagation along

the y-axis. Along the x-axis the width $\sigma$ is determined by two factors, the laser focal volume and the divergence of the molecular beam. The term $\sigma$ comes from the definition of a Gaussian, $f(v) \propto e^{-v^2/2\sigma^2}$. The latter of the two has been found to be a very minor correction since the width of the x-projection of $C_{60}^{+}$ and $C_{60}^{2+}$ are nearly identical $\sigma = 8.287$ pixels and 7.983 pixels, respectively. A constant velocity perpendicular to the time of flight axis results in a factor of $\sqrt{2}$ between single and double charge states for the same mass. The increase in spot size for the fragments can be attributed to the fragmentation process.

The fragmentation process of molecules occurs in three dimensional space. The 2D images, as shown in Fig. 5.21, are the projections of the 3D fragmentation onto a 2D plane, in other words, the integration over the z- (time of flight) axis. The 2D distributions were found to be independent of the z-axis (i.e., the left side of the mass peak produced the same 2D distribution as the right side which produced the same 2D distribution as a center portion), verifying the isotropic nature of the studied fragmentation. The 2D image can then be projected onto an x and y axis. The projection of the 2D image of each fragment image on the x and y axis, as well as the TOF mass peak, can be fit with a Gaussian, as shown in Fig. 5.23 for $C_{56}^{+}$. The Gaussian form has two interesting properties which are exploited in this work. The first is that the projection onto each axis can be considered separately. This is mathematically considered in Appendix B. The second property is that the width of a convolution of two Gaussians can be calculated by the sum of squares, i.e. $\sigma_{AB}^2 = \sigma_A^2 + \sigma_B^2$. It should be noted that the deconvolution was always performed in velocity space.

There are two ways in which the deconvolution can be made. The first deconvolution is given by

$$\sigma_N^2(real) = \sigma_N^2(measured) - \sigma_{60}^2(measured) \tag{5.9}$$

where $N$ denotes the fragment size with *real* being the deconvoluted width and *measured* being the experimental measured quantity. Here the apparatus width is removed from all particles by the subtraction of the width of $C_{60}^{z+}$, which results in an accumulated velocity.

The second deconvolution is given by

$$\sigma_N^2(real) = \sigma_N^2(measured) - \sigma_{N-2}^2(measured) \tag{5.10}$$

where $N$ again indicates the fragment size and $N-2$ indicates the previous fragment

size. This deconvolution assumes that $C_{60}$ fragments through sequential $C_2$ loss and results in a width associated with the last fragmentation.

The time scale for the fragmentation of the fullerenes is dependent on the initial internal energy and is known to occur up to the $\mu$s times scale. Fragmentation occurring outside the acceleration region ($> 2$ $\mu$s) is a concern for the 2D image, however, a close look at the time of flight distribution (Fig. 5.23b) shows only a slight asymmetry from a Gaussian function on the longer time of flight side. It is apparent that the majority of fragments are created in a small volume, and fragmentation outside the acceleration region will be neglected in this work.

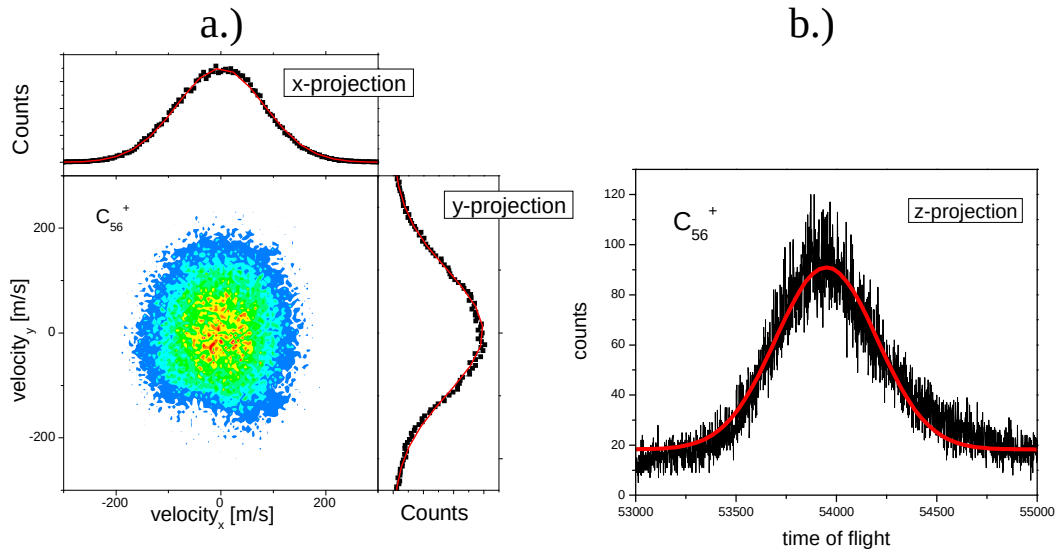


Figure 5.23: *Gaussian fit of the x-, y-, and z- projection of $C_{56}^{+}$ measured with a position sensitive detector. The laser conditions are the same as in Fig. 5.21. Here the zero velocities for* ***both*** *x and y components are set to the center of the Gaussian.*

The PSD maps the velocity distribution of the fragmentation process. The distance in pixels can be converted to velocity by the relation

$$v_r = \frac{r}{t_{C_n}} \tag{5.11}$$

where r is the distance from the center of the 2D distribution and is equal to $\sqrt{x^2 + y^2}$ and $t_{C_n}$ is the time of flight. The 2D projection is then projected onto either the x or y axis.

$$v_i = \frac{d_i}{t_{C_n}} \tag{5.12}$$

where $d_i$ is the distance from the center of the distribution for $i = x$ or $y$ , i.e., the number of pixels multiplied by the distance in mm per pixel. The time of flight of mass $C_n$, $t_{C_n}$, is given by the relation

$$t_{c_n} = \frac{L}{v_{z_{total}}} \tag{5.13}$$

where L is the length of the time of flight mass spectrometer and $v_{z_{total}}$ is the sum $v_z$ + $v_{acc}$. The acceleration velocity, $v_{acc}$ is dependent on the the charge, $Ze_0$, electric potential, $V$, and mass, $m$,

$$v_{acc} = \sqrt{\frac{2Ze_0V}{m}}. \tag{5.14}$$

The velocity due to fragmentation, $v_z$, is negligible in comparison to $v_{acc}$. Thus, the lateral velocity (perpendicular to time of flight axis) for x and y can be written as

$$v_i = \frac{d_p * N * \sqrt{\frac{2Ze_0V}{m}}}{L} \tag{5.15}$$

where $d_p$ is the width of the pixel, which is known geometrically to be 0.25 mm/pixels and $N$ is the number of pixels, the measured quantity. For a given voltage, this expression can be reduced to

$$v_i = b * N * \sqrt{\frac{Ze_0}{m}} \tag{5.16}$$

where $b$ is a constant of the experiment. In sections "kinetic energy release distribution: $C_{60} \rightarrow C_{58}$" and "Fragmentation by sequential $C_2$ loss", the voltage across the 2 cm interaction region was 500 V (with excitation occurring in the center), which leads to a $b$ value of

$$b = \frac{d_p * \sqrt{2V}}{L} = \frac{0.25 * 10^{-3}[m/pixel] * \sqrt{2 * 250[V]}}{0.45[m]} = 0.012423[\sqrt{V}/pixels]. \tag{5.17}$$

A second voltage which was used for results presented in this thesis (Section "Deviations from a single gaussian projection") was 1000 V. The corresponding $b$ value is

$$b = \frac{d_p * \sqrt{2V}}{L} = \frac{0.25 * 10^{-3}[m/pixel] * \sqrt{2 * 500[V]}}{0.45[m]} = 0.017568[\sqrt{V}/pixels] \tag{5.18}$$

The deconvoluted velocities for singly charged fragments in the x and y direction are shown on the left hand side of Fig. 5.24. The velocities have been calculated

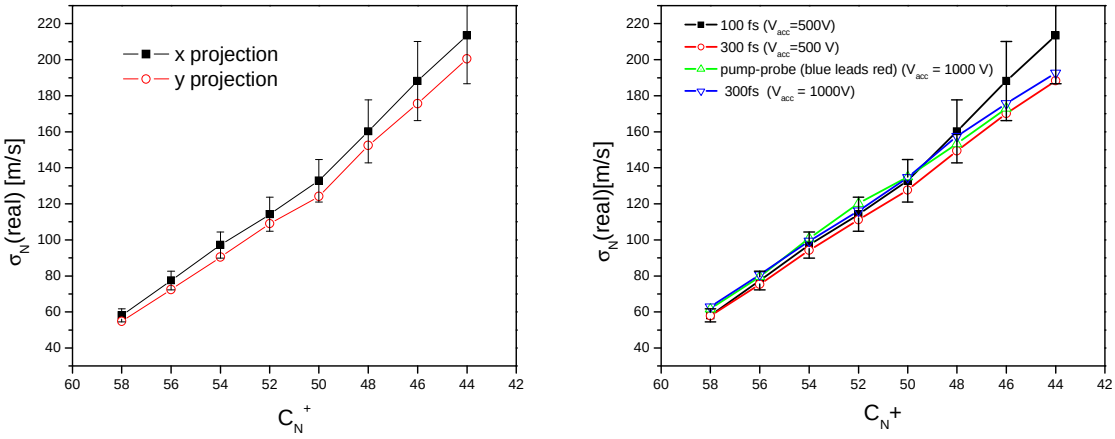


Figure 5.24: *Comparison of deconvoluted velocity widths of singly charged fragments. The deconvolution has been made according to Eq. 5.9. On the left, a comparison of the velocity widths for the x and y projections is shown. The excitation was with laser pulses of 100 fs pulse duration at 800 nm wavelength and with an intensity of 6*10$^{12}$ W/cm$^2$ (same as in Fig. 5.21). The ions were extracted with a voltage of 500 V. On the right, a comparison of the velocity widths (x projection only) for several different excitation and acceleration conditions is shown (see text for details). The error bars indicate the fitting error.*

following Eq. 5.9. The excitation source was a 100 fs, 800 nm laser with an intensity of 6*10$^{12}$ W/cm$^2$. The x and y axis projections are, to within error, the same.

On the right hand side of Fig. 5.24, the influence on the width of singly charged fragments for four different excitation and acceleration conditions is shown. The excitation was made with either a 100 fs, 800 nm pulse of intensity 6*10$^{12}$ W/cm$^2$ (full squares), or a 300 fs, 800 nm pulse of intensity 2*10$^{12}$ W/cm$^2$ (hollow circle), or a 300 fs, 800 nm pulse of 1*10$^{12}$ W/cm$^2$ (right-side up triangle), or a two color pump-probe scheme with a 400 nm pulse leading a 800 nm pulse by 2.5 ps (upside down triangle). The intensities of these pulses are estimated to be 10$^{11}$ W/cm$^2$ and 10$^{12}$ W/cm$^2$, respectively. The acceleration voltage for the first two cases was 500 V and 1000V for the last two cases. No significant difference is observed for the velocity widths with these four excitation and acceleration conditions.

Because of the similarity between the x and y projections as well as different excitation and acceleration conditions, only the x projection will be considered further in this work.

### Kinetic Energy Release Distribution: $C_{60}^+ \rightarrow C_{58}^+$

The first reaction to consider is the fragmentation of

$$C_{60}^+ \rightarrow C_{58}^+ + C_2 \tag{5.19}$$

This dissociation process has been frequently studied (for an overview see [MES01] and references within). In these works, the kinetic energy release distribution (KERD) of metastable fragmentation has been considered to determine the dissociation energy of fullerenes. The KERD of this fragmentation has been experimentally found to be

$$f(\varepsilon)d\varepsilon \propto \varepsilon^{1/2} e^{\varepsilon/k_B T} d\varepsilon \tag{5.20}$$

by Lifshitz [SLK92] and Märk [MES99b], where $\varepsilon$ is the kinetic energy and T is related to the internal temperature[1]. From Eq. 5.20, it is found that the energy distribution is dependent on the internal temperature. The energy distribution can be converted to a velocity distribution, which is shown in Eq. 5.21.

$$f(v)dv \propto v^2 e^{-v^2 m_r/2k_B T} dv \tag{5.21}$$

where $m_r$ is the reduced mass of the two fragment products. The relative velocity is related to the velocity of one particle by the relation

$$v_r = \left(\frac{m_1 + m_2}{m_2}\right) v_1 \tag{5.22}$$

The total velocity distribution of particle one is then given by

$$f(v_1)dv_1 \propto v_1^2 e^{-v_1^2 m_1/2k_B T} dv_1 \tag{5.23}$$

This distribution results when a Gaussian velocity distribution in Cartesian coordinates is assumed. The velocity distribution in each direction can be defined as,

$$f(v_i)dv_i \propto e^{-v_i^2 m_1/2k_B T} dv_i \tag{5.24}$$

for i= x,y, and z.

[1]In [MES99b], this is called the transistion state temperature, which is then related to an isokinetic temperature, which specifies the temperature for an infinite heat bath which would produce the same KERD. For the purpose of this thesis, it is sufficent to consider this as only a fit parameter.

Thus the total velocity distribution of particle #1 in Cartesian coordinates is given by

$$f(v_x, v_y, v_z)dv_x dv_y dv_z \propto e^{-v_x^2 m_1/2k_B T} e^{-v_y^2 m_1/2k_B T} e^{-v_z^2 m_1/2k_B T} dv_x dv_y dv_z. \quad (5.25)$$

The experimental projection onto a particular axis is the integration over the other two coordinates and is given by

$$f(v_x)dv_x \propto K' e^{-v_x^2 m_1/2k_B T} dv_x \quad (5.26)$$

where $K'$ is a constant from the integration over y and z. The only unknown parameter is $T$. The width is not affected by the constants of integration, and thus each dimension can be considered separately.

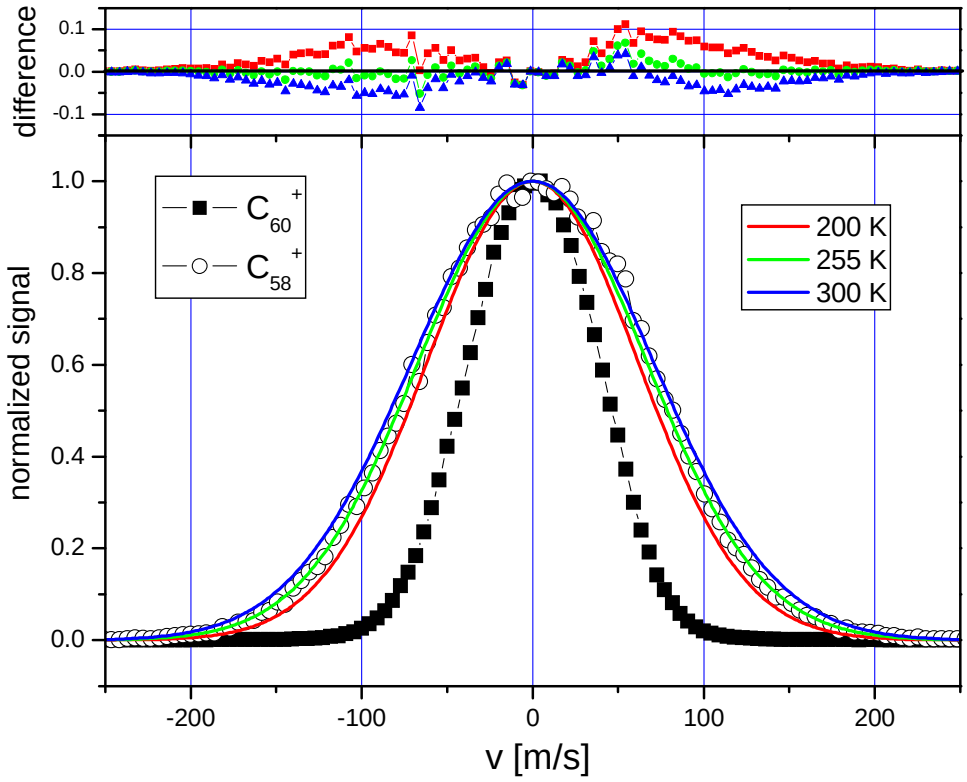


Figure 5.25: *The width of the $C_{58}$ fragment is determined by the convolution of the $C_{60}$ width and the velocity distribution of the fragmentation process. Three fit parameters are shown: $T$ = 200 K, 255 K, and 300 K. On the top, the difference is shown for each of the three fit parameters (squares - 200 K, circles - 255 K, and triangles - 300 K). The best fit is found for 255 K. The excitation of $C_{60}$ was with a 100 fs pulse of central wavelength 800 nm and intensity of $6*10^{12}$ W/cm$^2$.*

Fig. 5.25 shows the fit of $C_{58}^+$ using fit parameters of $T$ = 200 K, 255 K, and 300 K convoluted with the width of $C_{60}^+$ . The residuals between the experimental data and the three calculated distributions are shown at the top of the graph. The best fit was achieved with a fit parameter of 255 K ± 10 K.

From this fit, several quantities can be further extracted. For instance, the velocity at $1/\sigma$ of the Gaussian fit, for both $C_{58}^+$ and $C_2$, can be extracted from the fit.

$$\begin{aligned} e^{-v^2/2\sigma^2} &= e^{-m_{58}v_{58}^2/2k_BT} \\ \frac{1}{2\sigma^2} &= \frac{m_{58}}{2k_BT} \\ \Rightarrow \sigma &= \sqrt{\frac{k_BT}{m_{58}}} \end{aligned} \tag{5.27}$$

The lab frame velocity of $C_{58}$ ($v_{58x}$) is found to be 55.2 m/s. By momentum conservation,

$$v_2 = \frac{m_{58}}{m_2} v_{58}, \tag{5.28}$$

the velocity of $C_2$ ($v_{2x}$) is found to be 1601.1 m/s. The average kinetic energy in the laboratory frame of $C_{58}$ is defined as

$$\langle KER \rangle_{58}^{lab} = \frac{1}{2} m_{58} \overline{v^2} = \frac{1}{2} m_{58} \frac{\int_0^\infty v^2 v^2 e^{-mv^2/2k_BT} dv}{\int_0^\infty v^2 e^{-mv^2/2k_BT} dv} = \frac{3}{2} k_B T. \tag{5.29}$$

The corresponding kinetic energy release in the lab frame for $C_{58}^+$ is thus 33 meV. The lab frame kinetic energy can be converted to the center of mass kinetic energy by the relation (see Appendix B for details of the calculation)

$$\langle KER \rangle^{cm} = \frac{m_{58} + m_2}{m_2} \langle KER \rangle_{58}^{lab} = 0.99 \pm 0.09 eV. \tag{5.30}$$

The average kinetic energy release of 0.99 ± 0.09 eV found in the present measurements is significantly larger in value compared to values of the kinetic energy release measured from metastable fragmentation, $\langle KER \rangle^{cm}$ = 0.394 ± 0.014 eV [GME04a]. From work of Tomita et al. [TAH03], the kinetic energy release of $C_{60}$ molecules which decay at 1 $\mu$s has been estimated to be 0.497 eV (converted from temperature from Eq. 5.29). From RRK (or detailed balance) unimolecular fragmentation theory, the rate of fragmentation will be greatest for those molecules which have the most energy. Thus, by selecting a certain time window after excitation, one probes a small ensemble of molecules that becomes cooler as the time after excitation increases.

In the present measurement, all fragmentation events are recorded that occur within the fragments time of flight. In the results from Gluch, et al. [GME04a], only metastable fragments are measured and in the calculation of Tomita, et al. [TAH03], only a small time window of fragmentation is considered. Despite the differences in measurement techniques, the results are in qualitative agreement with known parameters.

### Fragmentation by Sequential $C_2$ Loss

In Fig. 5.21, the spatial distribution of the fragments are seen to increase with decreasing size. Table 5.1 presents the deconvoluted Gaussian fit width of the x-projection of several fragments both singly and doubly charged in terms of velocity [m/s] (the deconvolution of Eq. 5.9 was used). The non-zero width of $C_{60}^+$ has been discussed before (see Chapter 2) and is due to a combination of the molecular beam velocity and the focal region of the laser. This experimental width can be easily deconvoluted (see Appendix B).

To understand this trend, a statistical model has been applied to model the change in width of the measured spatial distribution versus the mass units lost. The model assumes the fragmentation process to be sequential $C_2$ loss from the fullerene, which will continue until the internal energy remaining in the system is insufficient to overcome the next dissociation barrier, or, more accurately, when the rate constant of fragmentation is greater than the experimental time window. Sequential $C_2$ loss is expected to fail for higher internal energy where fragmentation of larger $C_n$ fragments can occur, as has been observed in coincidence measurements [VHC98]. A general equation will be derived that is dependent solely on the number of fragmentation steps and known parameters. For details of the calculation, refer to Appendices A and B.

The philosophy behind the model is that each fragmentation step requires a certain amount of energy to surpass the dissociation barrier, in addition to the kinetic energy release (KER). Multiple sequential fragmentation steps are possible, as long as the internal energy of the remaining fragment is large enough to overcome the next dissociation barrier. However, the initial internal energy is unknown, or rather a distribution of internal energies exist [MHH03]. Thus, a trick is made where the final internal energy is considered to be the same for every mass size and the lost energy per fragmentation step is added. In other words, each fragment size is correlated to a

Table 5.1: *Velocity at $\sigma$ for several fragments x-projections for singly and doubly charged species. Values indicate the deconvoluted width (with respect to the $C_{60}$ width, i.e. Eq. 5.9) of the fragments. The instrumental width of $C_{60}^{+}$ was found to be 37.7 m/s and the width of $C_{60}^{++}$ was 51.31 m/s.*

| Charge | + | ++ |
|---|---|---|
| Fragment | width[m/s] | width[m/s] |
| $C_{58}$ | 55.2 ± 3.6 | 55.5 ± 3.6 |
| $C_{56}$ | 74.6 ± 5.2 | 77.1 ± 4.2 |
| $C_{54}$ | 93.4 ± 7.3 | 94.2 ± 12.0 |
| $C_{52}$ | 108.6 ± 9.4 | 113.1 ± 11.8 |
| $C_{50}$ | 127.1 ± 11.8 | 132.3 ± 16.1 |
| $C_{48}$ | 150.6 ± 17.5 | 150.5 ± 23.8 |
| $C_{46}$ | 170.3 ± 22.0 | 162.6 ± 25.9 |
| $C_{44}$ | 200.8 ± 26.7 | 170.4 ± 29.3 |

specific initial internal energy and the fragmentation distribution indicates the energy distribution.

The starting point is the average kinetic energy release of photoinduced unimolecular evaporation of clusters, which is, for systems with no reverse action barrier, given by Eq. 5.31 [Eng86, Eng87],

$$\langle KER \rangle = 2 * \frac{E_{int} - D}{s - 1} \tag{5.31}$$

where $E_{int}$ is the initial internal energy of the parent, $D$ is the dissociation energy, and s is the number of degrees of freedom. This quantity is calculated in the center of mass frame, and therefore special attention must be paid to transfer this to the lab frame for each fragment. After each fragmentation, the average accumulated KER

increases. The first fragmentation of $C_{60}$ is given by

$$\begin{aligned}\langle KER_1\rangle^{lab} &= \langle KER_{60}\rangle^{lab} + B_{58} * \langle KER_{60\rightarrow 58}\rangle^{cm} \\ &= \langle KER_{60}\rangle^{lab} + B_{58} * 2 * \frac{E_{int_1} - D_{60-58}}{s_1 - 1},\end{aligned} \tag{5.32}$$

where $\langle KER_{60}\rangle^{lab}$ is the "kinetic energy" associated with the non-zero width of the measured spatial distribution of $C_{60}$, and $B_{58}$ is the proportionality constant to change from the center of mass frame to laboratory frame, in which the average velocity of one particle is measured. The average velocity is given by the $\sigma$ of the Gaussian fit $e^{-v^2/2\sigma^2}$ of the measured velocity projection. The $B$ factor is found by conservation of energy and conservation of momentum considerations. Assuming $C_2$ loss, the B parameter is given by $B_i = \frac{m_2}{m_1+m_2}$, where $m_1$ is the mass of particle 1 and $m_2$ is the mass of particle 2 (see Appendix A for details of calculation). Thus, for $C_{58}$, $B_{58} = m_2/(m_{58} + m_2)$, where the indices here indicate the number of carbon atoms. The second fragmentation step is given by Eq. 5.33,

$$\begin{aligned}\langle KER_2\rangle^{lab} &= \langle KER_1\rangle^{lab} + B_{56} * \langle KER_{58-56}\rangle^{cm} \\ &= \langle KER_1\rangle^{lab} + B_{56} * 2 * \frac{E_{int_2} - D_{58-56}}{s_2 - 1},\end{aligned} \tag{5.33}$$

where $\langle KER_1\rangle^{lab}$ from Eq. 5.32 can be inserted into Eq. 5.33 giving Eq. 5.34.

$$\begin{aligned}\langle KER_2\rangle^{lab} &= \langle KER_{60}\rangle^{lab} + B_{58} * \langle KER_{60-58}\rangle^{cm} + B_{56} * \langle KER_{58-56}\rangle^{cm} \\ &= \langle KER_{60}\rangle^{lab} + B_{58} * 2 * \frac{E_{int_1} - D_{60-58}}{s_1 - 1} \\ &+ B_{56} * 2 * \frac{E_{int_2} - D_{58-56}}{s_2 - 1}.\end{aligned} \tag{5.34}$$

This calculation can be continued until $\Delta N$ $C_2$ units are lost and the remaining internal energy of the fullerene produces no further fragmentation on the time scale of the measurement. The only unknown parameter is the internal energy at each fragmentation step. Assuming the smaller fragment takes no energy and the KER is much smaller than the dissociation energy,

$$E_{int_2} = E_{int_1} - D_{60-58}, \tag{5.35}$$

which can be arranged to

$$E_{int_1} = E_{int_2} + D_{60-58}. \tag{5.36}$$

By "counting up" rather than down, one can assume solely a final internal energy, $E_{int_{final}}$, which can be constant for all fragments. Including this concept into Eq. 5.34, and generalizing the formula for $\Delta N$ fragmentation steps results in Eq. 5.37 (see Appendix A for details),

$$\langle KER_{total}\rangle^{lab} = \sum_{\Delta N=1}^{\Delta N} 2 * \frac{m_2}{m_{60-2\Delta N} + m_2} \frac{E_{int_{final}} + \sum_{\Delta N'=1}^{\Delta N} D_{60-2(\Delta N'-1)}}{173 - 6(\Delta N - 1)}, \quad (5.37)$$

where $\langle KER_{total}\rangle^{lab}$ indicates the total accumulated KER after $\Delta N$ fragmentation events, $m_{60-2\Delta N}$ is the mass of the larger fragment, $m_2$ is the mass of $C_2$, $D_{60-2(\Delta N'-1)}$ is the dissociation energy of the fragmenting particle, and $E_{int_{final}}$ is the final internal energy of a particular fragment, lying below the next dissociation barrier.

This model can be compared to either the accumulated kinetic energy release in the lab frame, $KER^{acc}_{lab}$ . The accumulated KER is calculated from the velocities deconvoluted using Eq. 5.9 where only the width of the $C_{60}$ is taken into account.

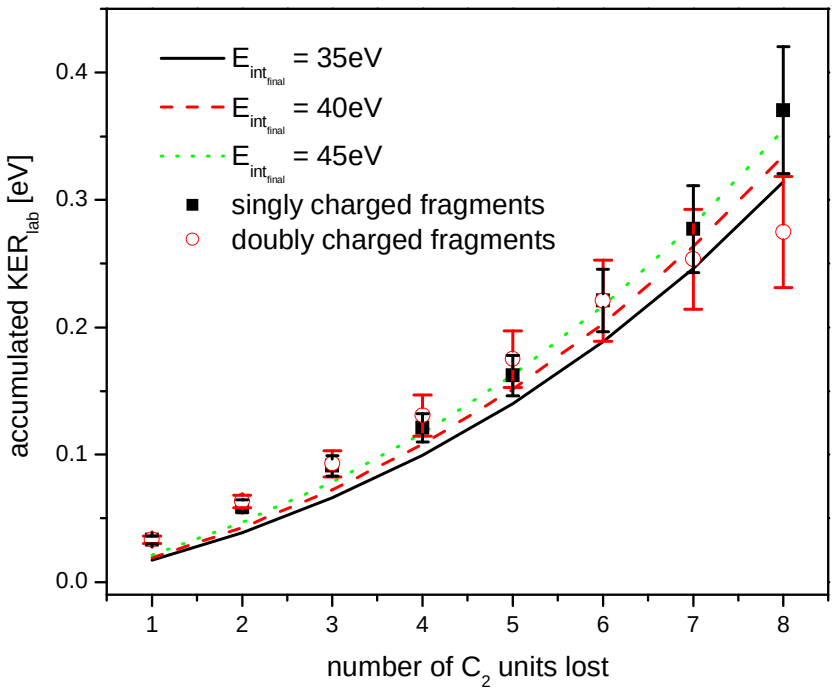


Figure 5.26: *Accumulated KER in the laboratory frame of $C_{58}$ versus the number of lost $C_2$ units for $C^{+}_{60-2n}$ and $C^{2+}_{60-2n}$. The excitation of $C_{60}$ was with 100 fs, 800 nm laser pulses of 6*10$^{12}$ W/cm$^2$. The experimental data are compared to a model assuming the sequential fragmentation of $C_2$ with three final internal energies of 35 eV, 40eV, and 45 eV.*

The accumulated KER in the laboratory frame of $C_{58}$, $\langle KER_{total} \rangle^{lab}$, is plotted in eV against the number of $C_2$ units lost and is presented in Fig. 5.26. Singly and doubly charged fragments are found to have nearly the same values of accumulated kinetic energy. This is in agreement with previous measurements [FES97]. The experimental values have been calculated by the procedure in Appendix B. The model of Eq.5.37 has been calculated assuming three different final internal energies, 35 eV, 40 eV, and 45 eV. These values were chosen since measurements indicate that the fragmentation thresholds for neutrals lies near these values.

The experimental values of $\langle KER_{total} \rangle^{lab}$ for larger fullerene fragments ($C_{58}^{z+}$,$C_{56}^{z+}$, and $C_{54}^{z+}$) are systematically larger than the model values. The widths of the smaller fragments are best fit with a final internal energy of 45 eV. The sequential $C_2$ loss model provides some evidence that a simple statistical model roughly describes the fragmentation of $C_{60}$ even after 100 fs laser pulse excitation.

The discrepancy for larger fullerene fragments may result from an underestimation of the final internal energies. As Fig. 5.23 indicates, fragmentation occurs primarily in the acceleration region. For $C_{58}^{+}$, this means the amount of time spent in the acceleration region is about 2 $\mu$s. The rate of fragmentation must be faster than this time. By Arrhenius estimations (see Eq.3.22), the initial internal temperature must be greater than 3500 K (using $A_d = 3.4 * 10^{21}$ and $E_d = 11eV$) in order to fragment on a sub-microsecond time scale. This corresponds to an internal energy of $E = 174k_BT = 53eV$, which is higher than the 35, 40, and 45 eV internal energies used.

However, this difference indicates that the model must be reformed. These reforms may include better account of energy loss upon fragmentation, i.e., including the energy lost due to the KER and/or internal energy of the $C_2$ unit and a higher final internal energy, as well as accounting for fragmentation which happens after the particle leaves the acceleration region.

### Deviations from a Single Gaussian Projection

Now that an understanding of the observed spatial distributions has been formed for the case of a single laser pulse of 100 fs, a comparison between different laser excitations can be made. Four different laser excitations will be considered, with an emphasis placed on the differences between a single laser pulse and a pump-probe excitation scheme. The motivation is from the additional KE observed in the pump-

probe scheme for small fragments, Fig. 5.17. The PSD would allow for a direct measurement of the kinetic energy release, perhaps illuminating the reason for the higher KE.

For the results presented in this section, a stronger acceleration field of 500 V/cm was used, resulting in a flight time of 50.7 $\mu$s for $C_{60}^{+}$ . A higher acceleration voltage was used to acquire more masses, since the TDC has a 32 $\mu$s time window. This stronger acceleration, however, reduces the spot size, since the time of flight is reduced. For comparison of spot sizes acquired with different acceleration voltages, a factor of $\sqrt{V_1/V_2}$ can be taken into account.

The spatial distributions were measured for clusters excited with either single pulses of 100 or 300 fs pulse duration with a fluence of 0.6 J/cm$^2$ or two pulses in a two color pump probe excitation scheme with a blue pulse of 3 $\mu$J and 110 fs pulse duration interacting with $C_{60}$ 2.5 ps before a red pulse of 27 $\mu$J and 110 fs pulse duration[2]. Under these laser conditions, an increase of small fragments, as discussed earlier in this chapter, was observed in pump-probe measurements when the 400 nm pulse is leading.

The mass spectra as measured with the PSD between 140 u and 370 u, are shown for four different laser excitation conditions in Fig. 5.27. Plot a.) results from pump-probe excitation with 800nm leading 400 nm by 2.5 ps, while plot b.) is a pump-probe mass spectrum with 400 nm leading by 2.5 ps. Plots c.) and d.) result from excitation with a single laser pulse of 300 fs and 100 fs pulse duration, respectively.

Fig. 5.27 highlights the m/z region where singly charged, doubly charged, and triply charged species coexist leading to uncertainty in the quantitative amounts of these species. In Fig. 5.27d, triply charged fragments can be clearly identified, as indicated by the arrows. These peaks are absent from all other spectra, indicating the highest charge state detected is 2.

A comparison of the spatial distributions resulting from excitation with a single laser pulse or with two pulses in a pump probe scheme will be made for all masses between 144 and 360 u in Fig. 5.27. A closer look into the x-projections of the spatial distributions is shown in Fig. 5.28 for $C_{58}^{z+}$ and $C_{48}^{z+}$, for z = 1 and 2, on a logarithmic-

[2]The spot size was unfortunately not measured for this laser configuration. It is assumed that the corresponding intensities are on the order of $10^{12}$ W/cm$^2$ for 800 nm and $10^{11}$ W/cm$^2$ for 400 nm, based on the pump-probe signal. The critical point is that they were overlapped and gave a pump-probe signal.

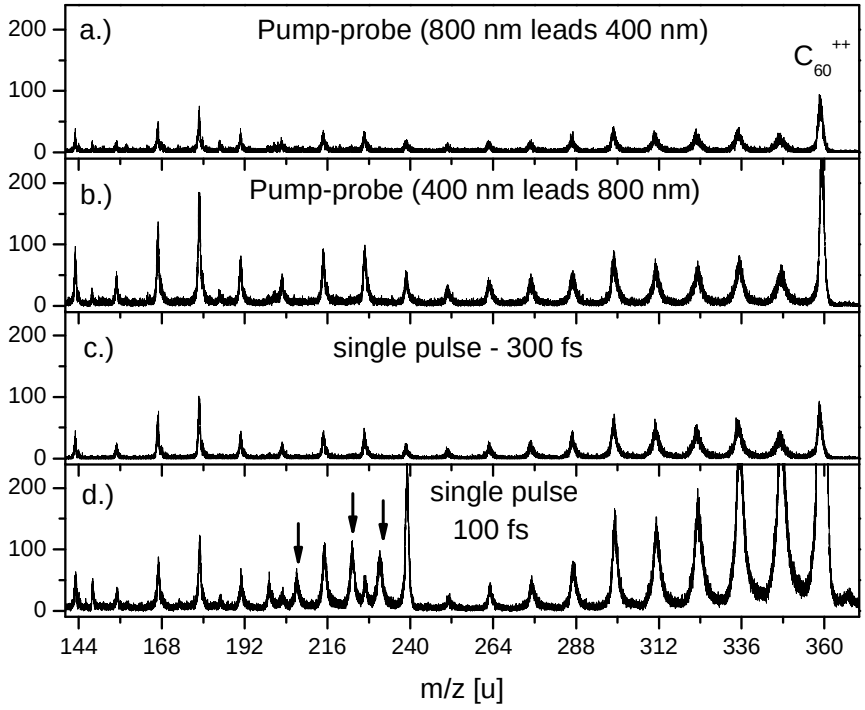


Figure 5.27: *Comparison of TOF mass spectra between 144 and 370 u for different laser excitations: a.) pump-probe configuration with 800 nm pulse leading 400 nm pulse by 2.5 ps, b.) same laser pulses, different order, c.) single laser pulse of 300 fs duration, and d.) single laser pulse of 100 fs pulse duration. The arrows indicate peaks that are unique to the triply charged state and do not overlap with fragments of different charge state.*

linear scale for a single pulse of 300 fs and for a pump-probe scheme with a blue pulse leading red pulse by 2.5 ps. The signals have been normalized to the maximum for a direct comparison. The singly charged fragments show no difference for any excitation scheme. The doubly charged fragments resulting from the pump-probe excitation show an enhanced width at the base in comparison to the single pulse of 300 fs pulse duration.

A closer inspection of the $C_{48}^{++}$ fragment, shown in Fig.5.29, shows that the underlying structure is also present for a single 100 fs laser pulse although not as strongly. The x-projections are fit with one, or, alternatively, two Gaussians. The fitting results for a single Gaussian are shown on the left hand side and are indicated by the dashed line in the graph. The fitting result from a sum of two Gaussians is displayed on the right hand side and is indicated by the dotted lines. Only one pump-probe excitation is shown since the projections were found to be independent of the order of pulses.

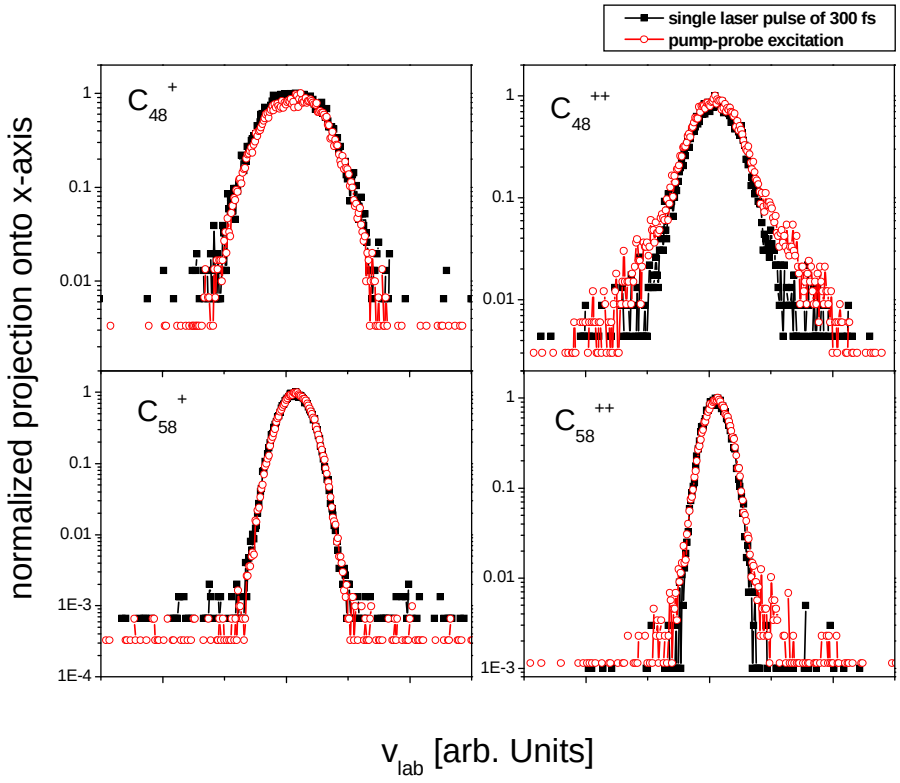


Figure 5.28: *A comparison of the x projection of $C_{58}^{z+}$ and $C_{48}^{z+}$, for z = 1 and 2 after excitation with either a single laser pulse of 300 fs and 3*10$^{12}$ W/cm$^2$ intensity (filled squares) or after excitation in a pump-probe scheme, with a 400 nm pump leading a 800 nm probe by 2.5 ps (open circles).*

The $\chi^2$ value is reduced for each excitation condition when a second Gaussian is used. In addition, the width of the narrow Gaussian is affected. Even with this consideration, the resulting width from 100 fs excitation is significantly wider than from either the 300 fs single pulse excitation or the pump-probe excitation, with a difference of approximately 30 m/s (∼330 m/s compared to ∼360 m/s). The width of the wider Gaussian is, within error, the same at a velocity of 900 m/s.

The double Gaussian nature of the projections indicates that there are two competing processes generating the structure of the mass projection. From the discussion about small fragments earlier in this chapter in section 5.2.1, the enhanced widths of the mass peaks of small fragments resulted from a Coulomb repulsion.

To further investigate the wider Gaussian, a dependence of the weight of each Gaussian on the m/z ratio is made. In this comparison, only the pump-probe exci-

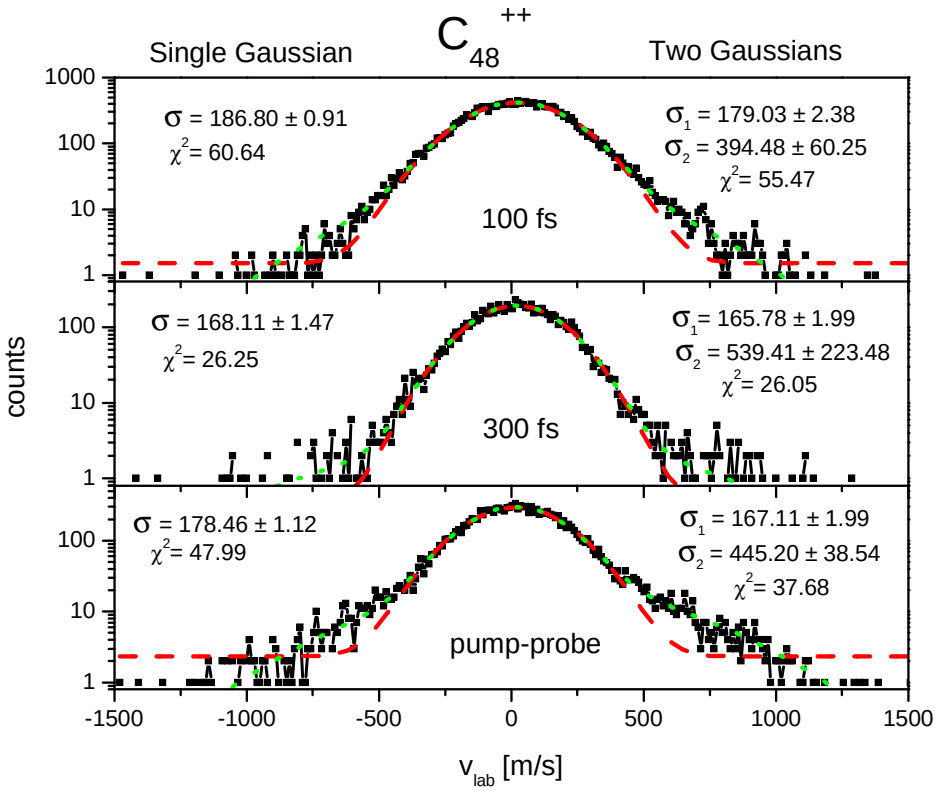


Figure 5.29: *A comparison of the x projection of $C_{48}^{++}$ after excitation with either a single laser pulse of 300 fs and 3*10$^{12}$ W/cm$^2$ intensity or after excitation in a pump-probe scheme, with a 400 nm pump leading a 800 nm probe by 2.5 ps. Since these values are not deconvoluted, they cannot be directly compared to the values in Table 5.1.*

tations from which the blue pulse leads the red pulse will be considered. Each of the x-projection peaks were fit with two Gaussians. A comparison of the amplitude of the two Gaussian widths is shown in Fig. 5.30 for several mass peaks. The widths are compared in Fig. 5.31.

The narrower Gaussian is found to dominate the projections in the region between 252 u and 348 u. The wider Gaussian becomes important for the lower masses shown in the graph. The narrow Gaussian fits for masses greater than 252 u can be explained by the typical $C_{2n}$ emission from fullerene-like fragments from doubly charged species. This trend can only continue to $C_{32}^{++}$ (192 u), however the $C_{2n}$ fragmentation channel is not expected to be significant beyond $C_{40}^{++}$ (252 u), as has been observed with single femtosecond laser pulses [THD00]. The trend of peak amplitudes of the wider Gaussian component (black bars in Fig. 5.30) is very similar to the mass distribution

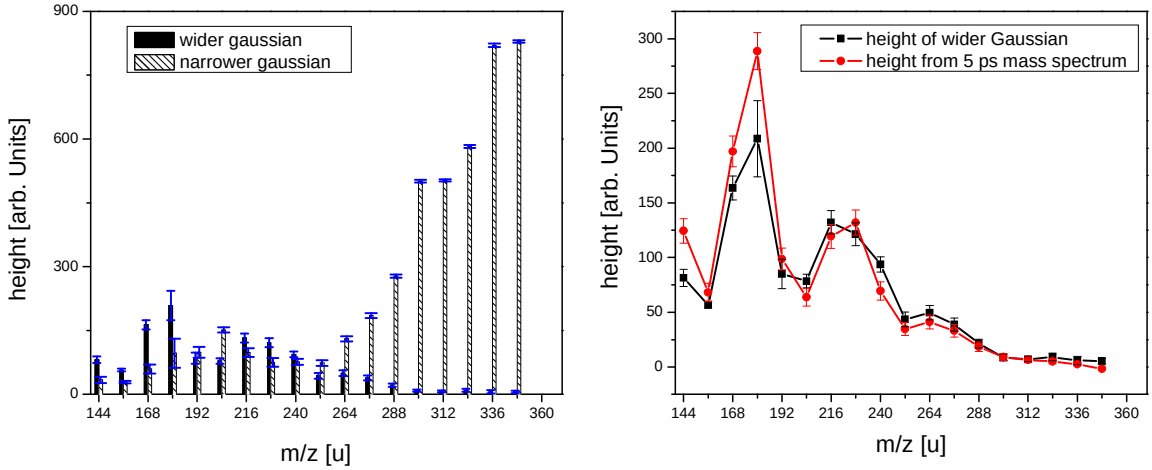


Figure 5.30: *On the left, a comparison of the amplitude of the two Gaussians fitting the x-projection versus the atomic mass units after excitation with 400 nm pump pulse leading an 800 nm probe by 2.5 ps. The bars filled with a striped pattern indicate the amplitudes of the narrower Gaussian and the filled bars indicate the amplitudes of the wider Gaussian. On the right, the amplitudes of the wider Gaussian are compared to the mass distribution after a picosecond laser excitation (same spectra as in Fig. 5.1.*

of singly charged ions between $C_{12}^+$ and $C_{29}^+$. Both $C_{15}^+$ (180 u) and $C_{19}^+$ (228 u) are significantly stronger than their neighbors and are so-called magic cluster sizes.

A comparison of the measured widths versus atomic mass unit is shown in Fig. 5.31a. The width (at $\sigma$ in velocity) increases nearly linearly for both species with decreasing fragment size, as indicated by the solid lines. The slopes of these two lines are equivalent.

In Fig. 5.31b, the ratio between the wider and narrower gaussian is plotted. The solid line indicates the ratio of the linear lines presented in Fig. 5.31a. As the mass increases from 144 u to 348 u, the ratio increases from 2.1 to 3.9. The calculated velocities of the wider Gaussian are more than a factor of two larger than those of the narrower Gaussian. However, assuming that the two Gaussians forming the spatial distribution are caused by an overlap of singly and doubly charged fragments (of the same m/z ratio) and assuming that the particles are emitted with the same kinetic energy (but different masses), the increase in velocity for the lighter fragment is only a factor of $\sqrt{2}$.

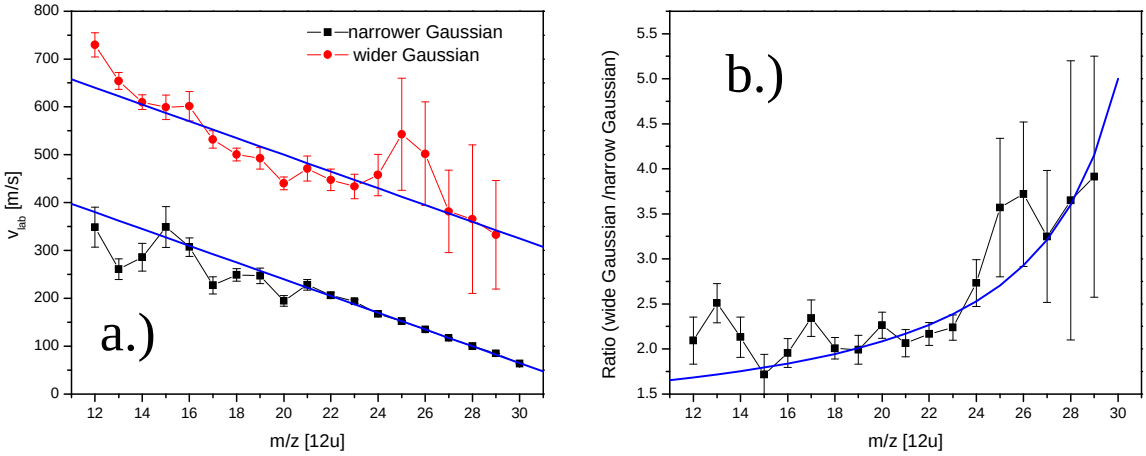


Figure 5.31: *a.) Comparison og the two widths (in velocity) of fragment masses between 144 u and 348 u. The solid lines indicate the linear increase of velocity with respect to the mass and that the two widths are separated by a constant value. b.) The ratio of the wider Gaussian to the narrower Gaussian is plotted. The solid line indicates the ratio given by the two straight, solid lines of a. The laser conditions are the same as in Fig. 5.30. These values also have not been deconvoluted and can be directly compared to Fig. 5.29, but not to Table 5.1.*

### Summary of Position Sensitive Detection

In the first part of this section, the kinetic energy release of the reaction $C_{60}^+ \rightarrow C_{58}^+ + C_2$ is considered after excitation with a 100 fs laser pulse of $6*10^{12}$ W/cm$^2$. A kinetic energy release of 0.99 $\pm$ 0.09 eV was determined. The kinetic energy release measured in this thesis is significantly higher than the kinetic energy release measured from metastable fragmentation. However, the value is not completely unreasonable considering that it is the integral over all fragments created in the first 2 $\mu$s with various amounts of internal energy, whereas in the measurements on the metastable fragmentation, a cooler ensemble is selected for analysis.

The second part of this section on the position sensitive detection of fullerene fragments a model with sequential $C_2$ loss from fullerenes is used to develop to predict the image size of different masses after $\Delta N$ fragmentation events using the known dissociation energies. A reasonable agreement is found for singly charged and doubly charged fragments (Fig. 5.26). The agreement of the model to experimental values supports that the fragmentation is predominantly a sequential $C_2$ loss for the fullerenes. Larger fragments ($C_4$, $C_6$, etc.) have been observed to be in coincidence

with smaller fullerene fragments [VHC98], however, this appears to be a minor channel.

A comparison of fragmentation lab frame velocities for various fragments with different laser excitations, either a single fs-laser pulse, or two laser pulses in a pump-probe scheme indicates that the widths for singly charged fragments ($C^+_{60-2n}$ ) are independent of the laser excitation method and can be fit by a single Gaussian. The doubly charged fragments exhibit a second component which is fit by a second, wider Gaussian. This wider Gaussian is most prevalent for the pump-probe excitation scheme.

Analysis of the amplitude of the two Gaussians indicates that the narrow Gaussian distribution can be assigned to sequential $C_2$ loss of doubly charged fullerene species, while the wider Gaussian distribution is attributed to singly charged fragments, since the fragmentation distribution mirrors that of single ps-laser pulse excitation. These species may arise after the multiple fragmentation of the cage after extreme heating.

This increased width is not likely to result from post-ionization of small neutral fragments because there is no obvious effect for the singly charged fragments (Fig. 5.28). The increased width is also observed for a single strong pulse of 100 fs, although to a lesser degree than the pump-probe in Fig. 5.29.

The position sensitive detector has illuminated important information about the fragmentation process of $C_{60}$ after excitation with 100 fs laser pulses. It is shown that the majority of fragmentation, even for these short pulse durations, can be interpreted through statistical models. It furthermore supports multiple fragmentation of the cage.

## 5.3 Summary and Conclusions

The fragmentation of fullerenes after femtosecond laser irradiation has been investigated in this chapter. Time-resolved pump-probe spectroscopy was used to investigate the fragmentation dynamics of $C_{60}$ after femtosecond laser excitation. A clear pump-probe transient signal is observed for all ions, with increased fragmentation occurring when a stronger (or blue) pulse leads the weaker pulse.

A time-dependent yield of the small fragments, particularly $C^+$, $C^+_2$, and $C^+_3$, is observed and shows an exponential increase with two time constants, one on the femtosecond timescale and the other on the picosecond timescale. However, these

time constants must be taken with a grain of salt, since the change of yield of these fragments has several sources. A further time dependence on the width of the small fragment mass peaks is observed. The change in width, which is related to the Coulomb repulsion of the fragments in the interaction region, gives further support that the fragmentation occurs on the time scale measured. The time domains observed with the small fragments push statistical theories to their limit. Fragmentation on a femtosecond timescale would be faster than the energy can completely redistribute. The dominant fragmentation mechanism leading to these small fragments is a multiple cage fragmentation of the $C_{60}$ molecule.

For the heavier fragments, the observed temporal dynamics occur within 1 ps, where a strong intensity dependence is observed for the groups of fragments $C^{2+}_{60-2n}$ and $C^{3+}_{60-2n}$ , as well as the mother ions $C_{60}$ , $C^{2+}_{60}$ , and $C^{3+}_{60}$ . The large, singly charge fragments, $C^{+}_{60-2n}$ , do not show this dependency. The fragmentation mechanism most responsible for these heavy fragments is sequential $C_2$ loss.

Further measurements are needed to further clarify the fragmentation dynamics for short delay times. A decisive experiment could be the use of femtosecond vacuum ultraviolet (VUV) laser pulses as a probe of the fragmentation event. The VUV pulses could ionize most fragments with a single photon, without significantly heating the vibrational system. This experiment was not performed because no VUV system existed during the course of this work, but is in present preparation at the Max Born Institute. The expected characteristics are 8.9 eV (140 nm) and 100 fs, which would provide adequate time resolution.

A second improvement would be to measure the photo-fragment-ions in coincidence. This would enable the possibility of distinguishing the fragmentation pathway. This coincidence measurement can be further improved by measurement with a position sensitive detector, where a complete mapping of the fragmentation process would be possible.

In the second part of the Chapter, the spatial distribution of the fragmentation of $C_{60}$ was investigated. The progression of widths with decreasing cluster size is modelled through statistical considerations and shows that sequential $C_2$ loss is the dominant mechanism producing the larger fullerene fragments. A second Gaussian component observed in doubly charged mass peaks is likely due to singly charged fragments created in a multiple cage fragmentation. The velocity is significantly larger than expected from a fragmentation of similar KER, perhaps indicating that a Coulomb repulsion is pushing the fragments apart.

It cannot be determined with the present measurements whether a non-statistical fragmentation channel exists. It is interesting that fragmentation with fs pulses is similar to fragmentation with nanosecond pulses, since the heating mechanisms may be different, i.e., a single electron excitation and relaxation or multiple active electrons.

These measurements are the first step toward making time resolved photo-ion photo-ion coincidence (or photo-electron photo-ion coincidence) experiments, which could provide further insight into fragmentation processes occurring on a ultrafast time scale.